NTNU – Trondheim
Norwegian University of
Science and Technology

Microstructure And Properties Of Extruded Al-Alloys For Crash Components In Cars

Nils Nortier Jensen

Materials Science and Engineering
Submission date: June 2014
Supervisor: Knut Marthinsen, IMTE
Co-supervisor: Svein Roger Skjervold, Sapa

Norwegian University of Science and Technology
Department of Materials Science and Engineering

Preface and Acknowledgment

The work in thesis was conducted at the Department of Materials Science and Engineering and at the Department of Structural Engineering, at NTNU. This study is part of a larger project initiated by Norsk Hydro/Sapa, and based on a student project on the crash properties of Al-Mg-Si profiles carried out at SIMLab, NTNU.

I would like to thank my supervisor Knut Marthinsen for his guidance throughout the work, and helping with theoretical aspects of the project. Furthermore I would like to thank Svein Skjærvold for providing the material studied in this work and for the needed background information and details for the project. Stephane Dumoulin also contributed with material, and should be mentioned.

In addition I would like to thank Pål Skaret for his assistance with the tensile testing, as well as Trond Auestad for helping with three-point bending test. Finally I would like to thank Trygve Schanche for his support in the metallurgy lab, and Yingda Yu for help with characterization by electron microscopy.

Abstract

The demand for lightweight materials in the transport industry is fuelling the research of high performing components. Extruded aluminium profiles intended for crash components are examined in this project. The objective in this work is to examine the microstructure and the mechanical properties, in order to further determine if the profiles behaves as expected. Both flat profiles and 2-chamber box profiles are studied.

Three Al-Mg-Si alloys: C20-Y1, C24-X1 and C28-C2 are inspected in this study. These are evaluated in three different tempers states: T4/W, T6 and T7. The characterization of the microstructure by light optical microscopy and scanning electron microscopy is completed. In addition, the mechanical properties of the materials are considered through tensile and bending tests.

The characterization showed a fully recrystallized microstructure in the C20-Y1 alloy, and fibrous microstructure in the C24-X1 and C28-C2 alloy. A typical deformation texture is observed in the two fibrous alloys. The recrystallized C20-Y1 alloy displays a strong cube texture. Large primary particles are present in the C28-C2 alloy, and the smallest particles are seen in the C20-Y1 alloy. For all alloys the particles are elongated in the extrusion direction.

C28-C2 displayed a loss of strength in T7-state compared to the other materials, presumably the highly alloyed profile reaches peak strength earlier. Reached true strain at max load by the recrystallized C20-Y1 is noticeably higher than the fibrous alloys. The true strain of this alloy is seen to be highly dependent of the temper state it is in. The fibrous microstructure is less affected by it temper state, which is likely connected to its subgrain structure. The C24-X1 shows the best bendability, assumed due to the combination of smaller primary particles and sub grain structure.

The flat profiles systematically reached the highest bending angles. It is also noticed the flat profiles consistently achieved higher true strain at max load in the T6- and T7-state. The 90-oriented specimens displayed highest bendability and highest true strain.

Sammendrag

Den store etterspørselen av lette materialer til transportindustrien driver forskning på høyt ytende komponenter. Ekstruderte aluminiumsprofiler tilregnet for kræsjkomponenter er undersøkt i dette prosjektet. Hensikten i dette arbeidet er å undersøke mikrostruktur og mekaniske egenskaper, for ytterligere fastslå om profilene oppfører seg som forventet. Både flate profiler og to-kammer boksprofiler er undersøkt.

Tre Al-Mg-Si legeringer: C20-Y1, C24-X1 og C28-C2 er vurdert i dette arbeidet. Disse fremkommer i tre forskjellige tempertilstander: T4/W, T6 og T7. Karakteriseringen av mikrostruktur er gjennomført med lys optisk og elektron mikroskopi. I tillegg er mekaniske egenskaper kartlagt ved strekk og bøy tester.

Karakteriseringen av materialene viste en rekrystallisert mikrostruktur i C20-Y1, i motsetning til de fibrige C24-X1 og C28-C2 legeringene. Typisk deformasjonstekstur er observert i de fibrige legeringene. Den rekrystalliserte C20-Y1 legeringen viste seg å bestå av kube tekstur. C28-C2 inneholder store primærpartikler, mens de minste partiklene er sett i C20-Y1. For alle legeringene er partiklene avlange parallelt med ekstruderingsretningen.

C28-C2 opplevde et styrketap i T7-tilstand sammenlignet med de andre materialene, som antageligvis skyldes at den høylegerte profilen når toppstyrke raskere enn de andre materialene. Den rekrystalliserte C20-Y1 nåde høyere sann tøyning ved maks last enn de fibrige legeringene, samtidig som at denne parameteren varier særdeles mellom tempertilstandene. Den fibrige mikrostrukturen er sett til å variere mindre, som sannsynligvis skyldes subkornstrukturen. C24-X1 viste beste bøyegenskaper antageligvis grunnet kombinasjonen av mindre primærpartikler og subkorn struktur.

De flate profilene nådde systematisk størst bøyevinkler. Det er også lagt merke til at de flate profilene konsekvent oppnådde høyst sann tøyning ved maks last i T6- og T7-tilstand. Prøvene orientert normalt på ekstruderingsretningen viste best bøyegenskaper samt størst sann tøyning.

Abbreviations

Acronym	Full name
CI	Confidence Index
EBSD	Electron Backscatter Diffraction
ED	Extrusion Direction
Eu	True strain at max load
Gb	Grain boundary
GP	Guinier-Preston zones
HV	Vickers Hardness
Ig	InterGranular
ND	Normal Direction
ODF	Orientation Distribution Functions
OIM	Orientation Imaging Microscopy
SD	Standard Deviation
SEM	Scanning Electron Microscopy
SIMLab	Structural Impact Laboratory
SSSS	Supersaturated Solid Solution
T4	Quenched and naturally aged
T6	Artificially peak-aged
T7	Artificially over-aged
TD	Transverse Direction
TEM	Transition Electron Microscopy
TS	True strain at max load
W	Temper a solid solution heat treated
XRD	X-Ray Diffraction
YS	True Yield Strength

List of Figures

List of Tables

Table of Contents

1 Introduction

The car industry's new demand for improved fuel efficiency in order to reduce the impact on global warming is emerging. Reducing the weight is therefore an objective for many car manufacturers. The search for lighter materials that can perform like steel is on going. Aluminium's specific weight is one-third of steel's and has good formability and corrosion resistance making it a suitable candidate for replacing steel structures in cars. A high efficiency of recycling also gives aluminium a great advantage in the long run. [1]

The car body is made of different components having different requirements with respect to material properties. Crash components need to able to resist shock in an efficient way. The material's strength and its ability to absorb energy are important parameters.

At the Structural Impact Laboratory (SIMLab) at NTNU, a project run in the summer of 2013 tested the properties of a number of partly new Al-Mg-Si alloys. This thesis is a continuation of a project performed by the author in the fall of 2013, and is also connected to a larger project with Hydro Aluminium/Sapa with a focus on crash behaviour of extruded aluminium alloys. [2]

The objective the current master thesis is to study the effect of the chemical composition and heat treatment of three Al-Mg-Si alloys. The materials are considered in three different tempers states: peak-aged T6, over-aged T7 and re-solutionized W/T4. In addition to the parameters mentioned above, the anisotropy in the mechanical properties is examined, as they are essential to the crash behaviour.

The discussion of this thesis is based on results obtained through different experiments. The experiments are supplemented with the characterizations of the different materials. With this in mind, a deeper understanding of the extruded profiles mechanical properties is sought.

2 Theoretical Background

The objective of this chapter is to give a general introduction of the important properties of extruded aluminium alloys. The three different 6xxx series aluminium alloys examined in this thesis are subjected to different production processes in accordance to the desired properties.

2.1 Thermo-mechanical processing

The thermo-mechanical processing of extruded profiles involves a number of different steps. As the name indicates this involves both heat-treatments and deformation methods. The process should be performed under controlled conditions to achieve desired properties. [3]

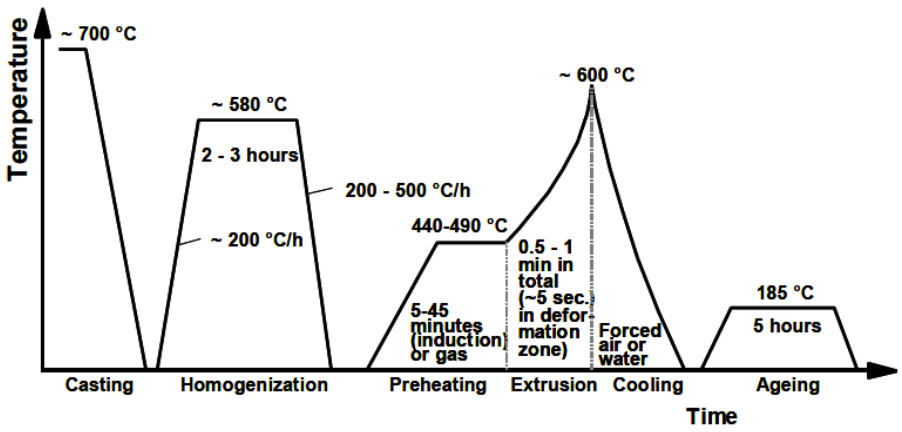

Figure 2-1: Sketch of the thermo-mechanical processing of extrusions with the temperature as a function of time. [4]

Figure 2-1 illustrates the temperature as a function of time, a schematic representation of the production process.

First the aluminium is cast, then it is homogenised to remove unwanted segregations of alloying elements and composition differences throughout the thickness of the billet. Then the billet is preheated, extruded and cooled. Finally the extruded product is aged to achieve the required final properties.[3]

2.2 Extrusion

Extrusion is a process used to change the size and shape of cast billet to a desired profile. The billet is forced by a ram through a die making a continuous length cross-section product, illustrates in Figure 2-3. This is generally performed at higher temperatures to reduce the flow stress of the material, lowering the power requirements. The process can also be done cold in some instances. [3]

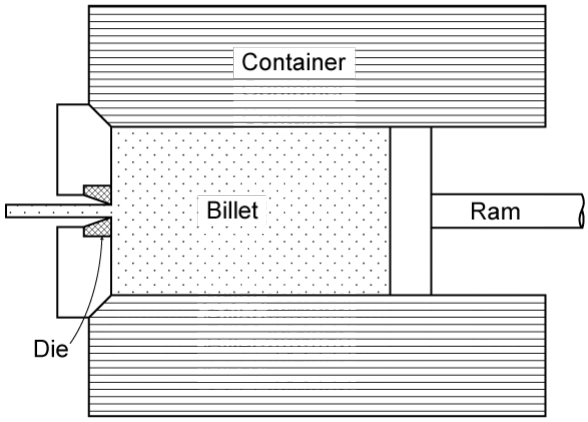

Figure 2-2: Extrusion of an aluminium billet (adopted from [5], figure 18-1 page 617)

Extrusion allows for creation of exceedingly complex shapes, making it a much used industrial process. The process greatly affects the properties and microstructure of the material. In order to control the structure of the material, the whole thermo mechanical process should be considered. [3]

2.3 Work hardening

During deformation of aluminium alloy, dislocations generate and multiply. This leads to the creation of dislocation tangles, sub-grains or cells that increases the strength of the alloy. In this section the fundamental mechanism of work hardening will be discussed. [6]

Work hardening is a consequence of the fact that dislocations movement becomes increasingly hindered during deformation. Solute atoms, other dislocations, dispersed precipitates and grain boundaries act as obstacles. In order to further understand the mechanisms of the work hardening, the chronological stages will be explained. [7]

In the first work hardening stage, the dislocations do not interact with each other and the work hardening rate is low. In fact this stage is almost negligible for polycrystals, as dislocation movement is constrained by the grain boundaries. [7]

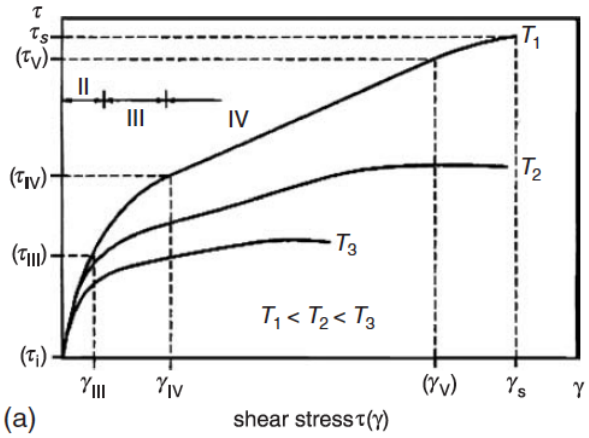

Figure 2-3: Different work hardening stages. [7]

In the second stage of work hardening, the dislocations starts to interact with each other on different slip systems. The dislocations multiplication occurs rapidly leading to a large work hardening rate. The work hardening rate remains constant due to mechanisms like grain boundary pile-up, requiring an increasing amount of stress to further move the dislocations. Stage II can last to about strains of 0.05 to 0.2 depending on the material.[7]

As the material enters the third stage the work hardening rate decreases significantly and the flow curve gets a parabolic shape. Local dislocation annihilation starts equalize the dislocation multiplications. Dynamic recovery like cross-slip allow the dislocations to move more freely and equally opposed dislocations delete each other. [7]

In the fourth and last stage the work hardening remains low and constant, but lasts over large values of strain. [7]

In solid solution certain alloying elements are attracted to dislocation cores. Increasing the strength of the material by obstructing the dislocation movement. The atom size plays a role on the effectiveness of the solute-dislocation interaction. Larger solute sizes create an attractive force to the dislocation. [7]

If the size of alloying element is similar to the atoms of the matrix, the shear modulus becomes significant. In that the shear modulus of the matrix with a solute concentration creates an additional energy interaction. [7]

2.4 Recrystallization and recovery

During extrusion at low temperatures the metal is subjected to a large amount of plastic deformation. A large amount of work used to shape the material is released as heat during the deformation, and approximately 1% stored energy remains in the material. The stored energy emerges mainly as dislocation at ambient temperatures. Annealing subjects the deformed material to a change in microstructure. The release of the stored energy during annealing is the driving force for recovery and recrystallization. [8]

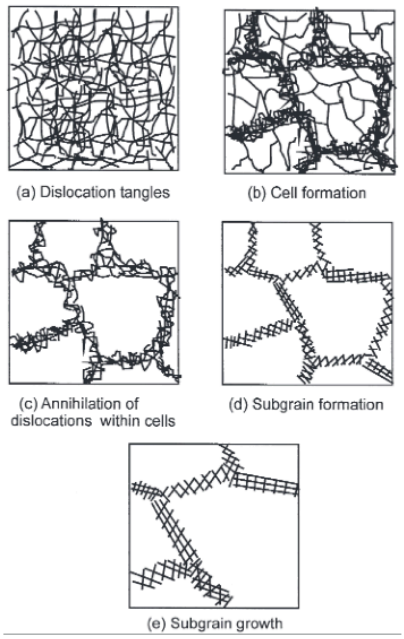

Figure 2-4: Recrystallization of deformed microstructure. [8]

For extruded aluminium alloys the heavy deformation affects the microstructure. Recovery can be described as series of steps to partially restore properties of the material before deformation. By migration and annihilation of dislocations the stored energy can be lowered. Before annealing, the deformed material will contain a high density of dislocation tangles. Recovery occurs when the dislocation rearrange into cells. The dislocations inside these cells are then annihilated. Finally the cells dislocation boundaries are rearranged to form stable sub-grains, and eventually growing in size. It should be noted that recovery can occur during the deformation process at high temperatures, known as dynamic recovery. [8]

Recovery and recrystallization can occur simultaneously, when these are competing processes. If the material is fully recrystallized and all the deformation structure is consumed, no more recovery is possible. At the same time, if a large amount of recovery has “been done”, the driving force for recrystallization is lowered. [8]

The term recrystallization is usually refers to nucleation of strain free grains which consume the deformed or recovered microstructure. It is important to distinguish this phenomenon from abnormal grain growth, which may occur in fully recrystallized material. Furthermore recrystallization can be separated in to two steps: nucleation and growth. [8]

Nucleation of strain grains occurs in deformed heterogeneities like grain boundaries, transition bands and shear bands. In other words, materials subjected to large strain will provide more possible nucleation sites than a material with low strain. [8]

Before detailing the recrystallization and recovery process, the grain boundary hardening phenomenon should be mentioned. The cell substructure gives an increase in strength defined by the Hall-Petch type having the form of:

$$\sigma = \sigma_0 + k_1 d^{-m} \qquad \textbf{(2-1)}$$

Where σ is the yield strength, σ_0 is the frictional or Peierls stress, k_1 denotes the strength of the cell boundaries and m is a constant. The walls of these cells are made of entangled dislocation. Depending the temperature during extrusion the cells can become subgrains. These give a increase in strength over cell substructure. The increase in strength also gives a loss in ductility compared for example a recrystallized microstructure. [6]

2.5 Age hardening

The age hardening processes can be explained by splitting it into stages. First the alloy is heated to a single-phase region to dissolve the alloying elements. This first step is called solution heat treatment. Then the alloy is quenched to room temperature to create a supersaturated solid solution (SSSS). By rapidly cooling the aluminium, the alloying elements become “trapped” as a solid solution, and in addition a lot of vacancies are “quenched-in” that may facilitate subsequent diffusion processes. The third step involves heating the alloy to a medium high temperature known as ageing. This step allows the alloying elements to precipitate as finely dispersed particles. [6]

In many cases he ageing procedure of heat treatable wrought alloys is more elaborate than previously described. The Al-Cu system however is often used as an example to get a better understanding often the ageing process.

The development of Guinier-Preston (GP) zones is typically the first step. GP zones are clusters of alloying element atoms. These clusters are of one or two atom plane thickness. When the alloy is quenched, all the Cu alloying elements remain in solid solution. Vacancies are also trapped during quenching, and they assist the movement of the alloying elements. GP zones are coherent with the structure of the matrix, but often produces elastic strains in surrounding matrix. This phenomenon gives increase in hardness. [6]

By ageing the Al –Cu alloy, the diffusion rate increases. GP-zones are the first precipitates produced. The next phase to be produced is the metastable θ'' phase. This phase grows from the GP-zones, and eventually replaces the former completely. Formation of this phase gives a new increase in hardness. The exact composition of the θ'' phase is still not determined. [9]

With further ageing of Al-Cu, a decrease in strength starts to develop. A new phase, the θ'-phase, replaces the θ''-phase. This new phase nucleates on dislocations or similar heterogeneities. This loss of hardness is called over-ageing and is partly due to a change from coherent to incoherent precipitates, which also leads to a transition of shearing of particles to looping. Moreover a general coarsening of the particle structure will take place. [9]

The last part of the precipitation sequence is the production of the stable equilibrium phase θ. This phase has the composition Al2Cu.

For an Al-Mg-Si alloy, the general precipitation sequence can be given as:

SSSS-> GP -> β'' ->β' -> β (MgSi) [9]

- GP: Assumed to be magnesium and silicon, with a monoclinic structure. [9]
- β'': Monoclinic, assumed to be Mg5Si6, although it's been argued that the phase also may contain some aluminium. [9]
- β': Hexagonal structure. Al-Mg-Si alloys with maximum hardness contain a mixture of β'' and β'. [9]
- β: Mg2Si, Cubic incoherent phase. [9]

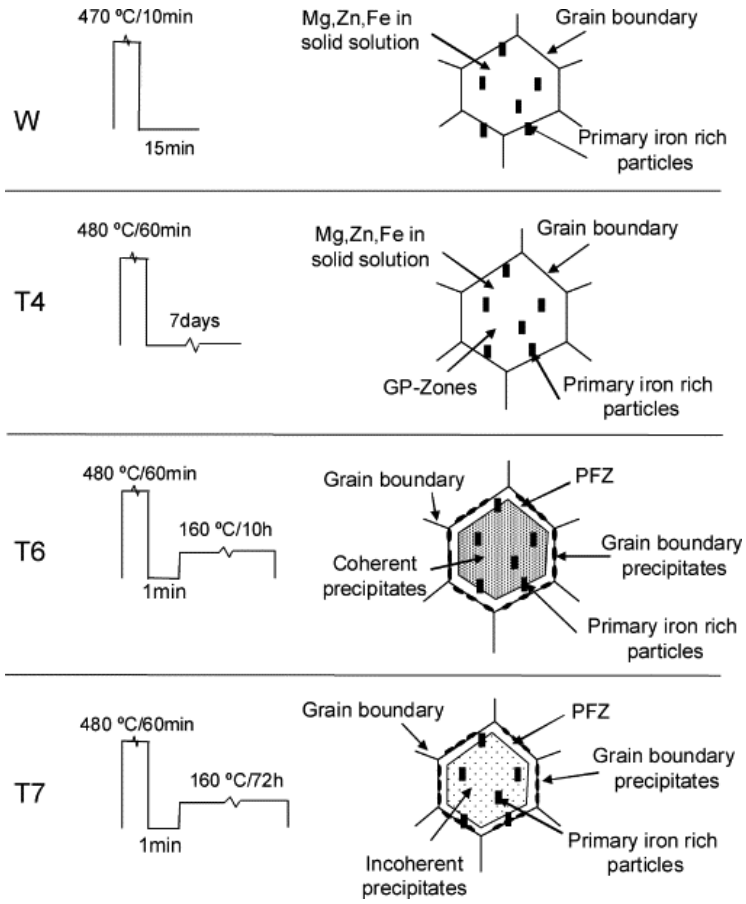

Figure 2-5: Schematic representation of the precipitation structure in the different tempers in AA7030. [10]

The designation of the tempers is important. After being quenched from the single phase region, the material has the temper W. The material can be naturally aged in room temperature to get the temper T4. If the material is aged at an elevated temperature the precipitation of finely dispersed particles. Alloys can be aged to maximum strength are given the temper T6 or can be over-aged to T7. Figure 2-5 is used to illustrate the precipitation in an 7xxx aluminium alloy.

The dislocations interaction with the secondary particles is the source of the strengthening. The particles can act as barriers to the dislocations in different ways. They can either cut through or “move around” the particles. Small and/or soft coherent particles have large affinity to be cut and deformed. [5]

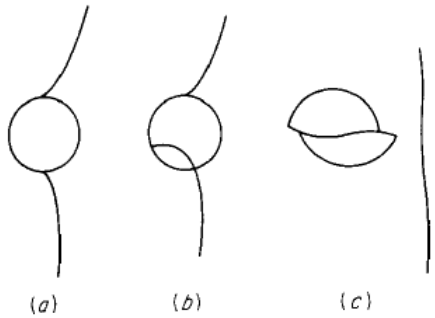

Figure 2-6: Particle cut by a dislocation. [5]

Orowan proposed a mechanism of interaction for incoherent particles and dislocations. The dislocation line bows around the particles instead of cutting them. When the dislocation line reaches a critical curvature, the line on each side of the particle is of opposite sign allowing annihilation. This leaves a loop around the particle. This mechanism is shown in Figure 2-7. [5]

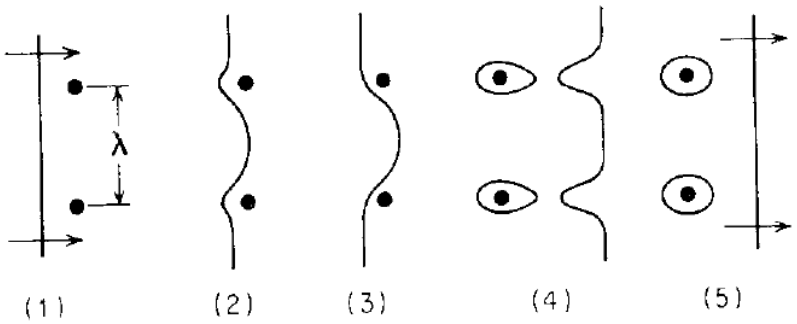

Figure 2-7: Orowan mechanism. [5]

Before continuing to next section, the effect of the alloying content on the heat-treatable Al-Mg-Si alloys should elaborated. In commercial alloys the content of Mg and Si is often "balanced" to form quasi-binary Al-Mg_2Si alloys. Generally the alloys can divided in to three groups based on the amount of Mg and Si.

1. Balanced amounts of Mg and Si between 0.8% and 1.2%, moderate strength is achieved [6]
2. Excess of 1.4% Mg and Si. These are more quench sensitive develop higher strength on ageing. Cu is often added to enhance mechanical properties together with 0.2% Cr to offset adverse effect Cu may have on corrosion resistance. [6]

3. Excess of Si than needed to form Mg_2Si. The presence of excess Si promotes an additional response to age hardening, by both refining the size of the Mg_2Si particles and precipitating as Si. This may reduce ductility and cause intergranlar embitterment as Si segregates to grain boundaries. The addition of Cr and Mn helps counter this effect by promoting fine grain size and inhibiting recrystallization during solution treatment. [6]

2.6 Texture

The texture of a material designates the orientation of the grains. A material containing grains with random orientations is said to have no texture or a random texture. In most cases the grains are not random, and will have a crystallographic texture. The development of texture can be related to several different processes. Deformation, recrystallization and grain growth will also generate texture. [7]

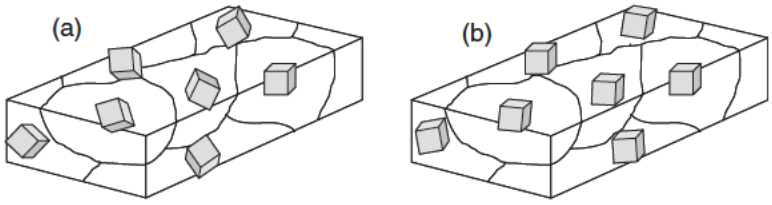

Figure 2-8: Materials (a) with and (b) without texure [7]

In order to represent the texture of the grains, a co-ordinate system need to be defined. The direction of extrusion is used as a reference for the orientation of the grains. Extrusion Direction (ED), the Normal Direction (ND) and the Transverse Direction (TD) are defined in Figure 2-9. Miller indices are utilized to define the crystal orientations, and are written: {hkl} for planes and <uvw> for directions. For extruded specimens only the <uvw> direction is used to describe the texture, and should be parallel to ED. With this co-ordinate system, different representation methods can be used. [7]

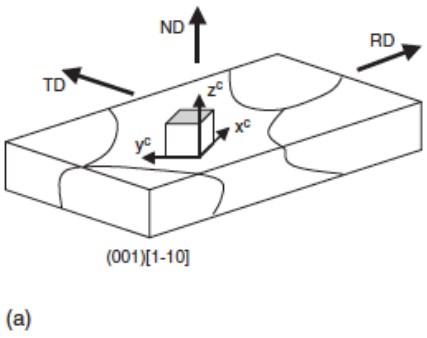

Figure 2-9: Orientation of ED, TD and ND. [7]

Pole figures is a tool utilized to represent texture by stereographic projections. By choosing a particular set of crystallographic orientations e.g. all the <100> directions, the <100> pole figure can be plotted.

The sample is placed in the centre of the sphere, with ND pointing towards the north pole, Figure 2-10(a). Then a set stereographic direction is projected on the equatorial plane. Only directions in the northern hemisphere are projected. Then a pole figure can be represented like in Figure 2-10(b). A pole figure with projection scattered randomly is said to have no texture. In most cases the projection of orientations cluster in certain areas, giving a sharp texture.

Although it's important to note that to determine the texture form an experimental polefigure analysis isn't always straightforward. The simplest way to confirm results is to compare them to standard pole figures like Figure 2-11. Some of important texture components are (b) Brass, (d) Cube and (e) Goss.

Pole figures are usually shown with contour lines to illustrate the concentration of the distribution seen in Figure 2-10(e), instead of single points. It's important to note that comparing pole figures can be misleading, and that the intensities of the contour lines need considered. [7]

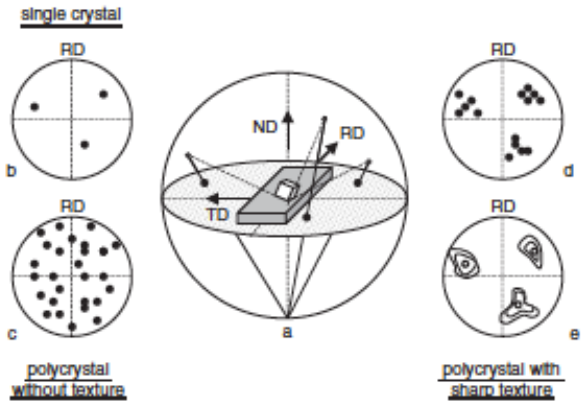

Figure 2-10: Pole figures of a single crystal and polycrystal [7]

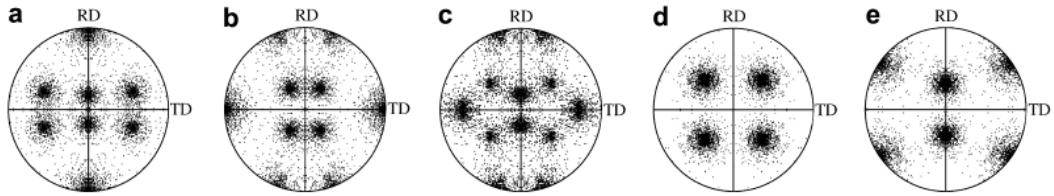

Figure 2-11: Examples of typical 111 pole figures in aluminium. (a) Copper, (b) Brass, (c) S-texture, (d) Cube and (e) Goss. [11]

An orientation distribution function (ODF) is another tool used for a graphical representation of texture. ODF is a mathematical expression to describe the texture of a sample. In this section a short explanation of the theory behind ODFs will be given. [7]

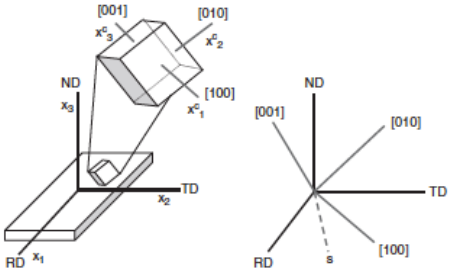

Figure 2-12: The Euler Angles [7]

To represent the texture graphically a coordinate system must be defined to relate the orientation of the sample and the grains. Figure 2-12 shows a randomly oriented grain in sample. The X_i coordinates relate to the sample axis and X^c_i coordinates relate to the grain orientations. In the literature different condition can be used to relate both coordinate systems. In this case the system of Bunge will be used. By rotating the X^c_i system around RD, TD and ND the orientation of the grain can be related to the sample. These three rotations are called Euler angles. The angles φ_1, Φ and φ_2 relate respectively to RD, TD and ND. [7]

Further these angles can be plotted in Cartesian coordinate system called the Euler space. This space can graphically represented as a cube, with Euler angles as the axis. This cube "contains" all the different crystal orientations. [7]

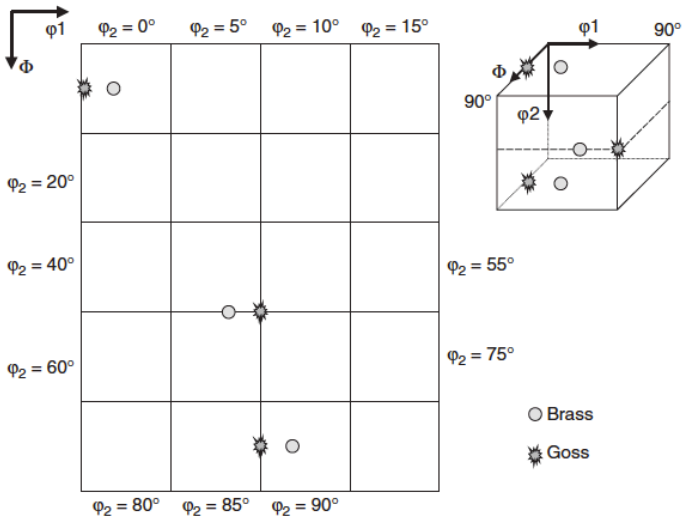

Figure 2-13: ODF and the Euler space [7]

The Euler space is difficult to represent directly due to the 3 dimension of the cube. Therefore the cube is broken down a square, with φ_1 and Φ as the axis. Maps of these squares are given for φ_2 different angles. The 2D representation of an ODF is shown in figure Figure 2-13. [7]

It's important to note that the same crystal orientation can be represented with different angles in the Euler space due to symmetry. A typical ODF of a strongly deformed fcc material (like aluminium) is shown in Figure 2-14, with the corresponding textures.

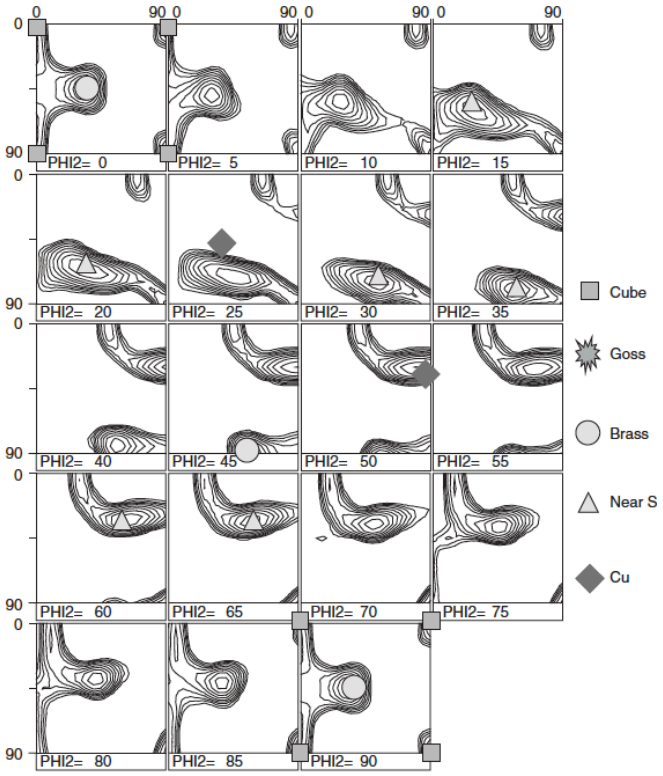

Figure 2-14: Typical ODF of a deformed texture in Al (cold rolled) [7]

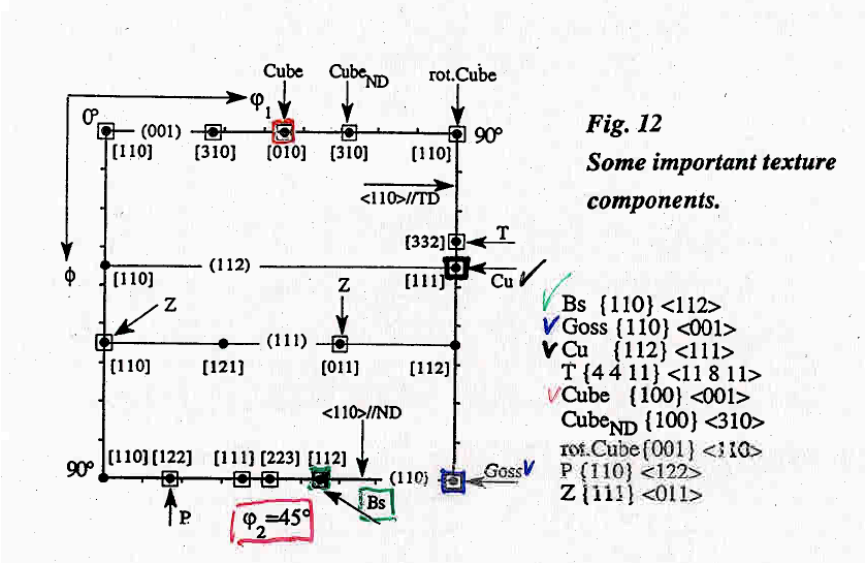

Figure 2-15: More texture components for ϕ_2=45°. [12]

Much of the literature on crystallographic texture focuses on plane strain condition trough out the thickness of the profiles. This is rarely occurs in practice. It is thought that texture heterogeneity becomes more pronounced under conditions of high friction. An often seen shear texture in Fcc-metals include {001}<110> -component. [8] [13] This texture component is known as Rotated cube texture. Figure 2-15 shows the component in the $\varphi_2 = 45°$ section of the ODF, in the two top corners.

2.7 EBSD

Electron backscatter diffraction (EBSD) is a versatile characterization technique. Individual grain orientation, local texture, phase identification and more can be determined. Scanning electron microscopes (SEM) can be equipped with an EBSD detector allowing for microstructure analysis in great detail. [14]

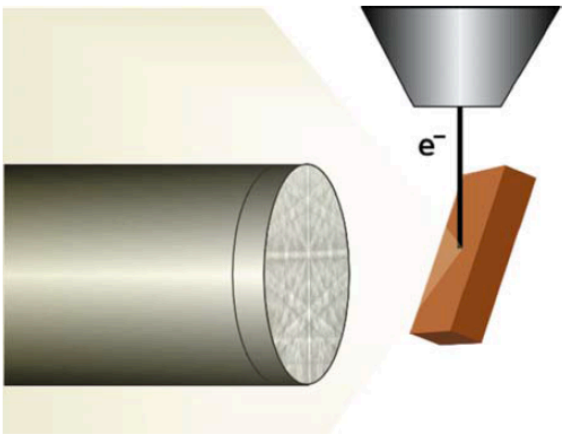

Figure 2-16: Representation of the EBSD method, showing the diffraction patter no the phosphorus screen [14]

The method generates a diffraction pattern that is used to characterize the surface of a sample. When a stationary beam hits a surface at an angle, the backscattered electrons interact with the atomic planes, Figure 2-16. This produces a diffraction pattern containing characteristic Kikuchi bands. The backscattered Kikuchi pattern and the interplanar spacing (d_{hkl}) can be related be Bragg's law, equation (2-2). [14]

$$2 \cdot d_{hkl} \cdot sin\theta_{hkl} = n \cdot \lambda \qquad \textbf{(2-2)}$$

θ_{hkl} is called Braggs angle, which is the angle of the incident beam and the atomic planes. λ is the wavelength defined as a function of the acceleration current of the electron beam, equation (2-3). [15]

$$\lambda = \frac{12{,}24}{\sqrt{E_0}} \qquad \textbf{(2-3)}$$

The patterns of Kikuchi bands are used to determine the crystallographic orientation of a grain. The Kikuchi bands are a projection of the lattice planes. For cubic crystals the origin of

a band is determined with the equation (2-4). Here, *a* is the lattice parameter and *h*, *k* and *l* are the Miller indices of the atomic plane. [15]

$$d_{hkl} = \frac{a}{\sqrt{h^2 + k^2 + l^2}} \quad \textbf{(2-4)}$$

Experimentally the EBSD method is done by placing the sample in SEM chamber and tilted. With EBSD detector inserted, the acquisition of diffraction patterns can be done. Then the patterns are the indexed in post-processing program, to determine the orientation of the grains. [14]

2.8 Z-contrast

Z-contrast is characterization technique used to detect different phases of the microstructure. Metallic alloys placed in a SEM emit both backscatter and secondary electrons. The fraction of backscattered electrons of a sample varies from phase to phase. [15]

$$C = \frac{S_2 - S_1}{S_2} \quad \textbf{(2-5)}$$

The recorded contrast is directly related to the atomic number. A phase with a high atomic number will give of a stronger signal than a phase with a low atomic number. The contrast is defined in equation (2-5), where S_2 is the signal emitted from the phase highest atomic number and S_1 the opposite. C is by convention positive and represents the information in the signal that can be related to samples properties. [15]

2.9 Tensile properties

The mechanical properties of materials can quantitatively be measured and represented by different methods. The tensile test gives a good overview of the mechanical properties, in the form of stress-strain curves. The test is performed by applying an external loading on a specimen. The load is uniaxial to the length of the specimen, and is increased the point of fracture. The Figure 2-17 shows a typical stress-strain curve. [16]

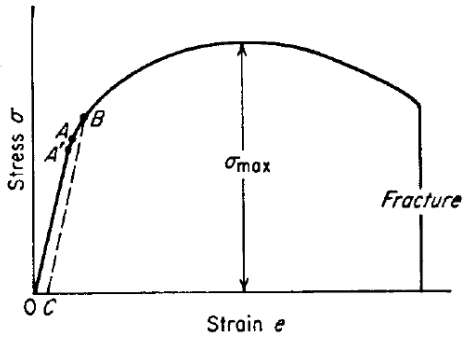

Figure 2-17: Stress-Strain curve of a ductile material. [5]

The applied stress increases linearly at low strains, up to the yield strength. Until this point the material only deforms elastically, and if the applied stress is removed the specimen retracts to its original shape. After this point material deforms plastically, i.e. the shape of the specimen is irreversibly deformed. For ductile materials like aluminium, the required strength after yield is increasing for each strain increment. The maximum strength is called the ultimate tensile strength.

$$\sigma = \frac{P}{A_0} \tag{2-6}$$

$$\varepsilon = \frac{l - l_0}{l_0} \tag{2-7}$$

The stress is defined as the applied load P divided by the original area of the cross section. The strain is the elongation relative to the original length. When these are plotted against each other they give the engineering curve. However, this curve does not take into consideration the plastic deformation of the material, only the original dimensions. As the specimen's strain increases, the cross-section area will decrease and length increases. The formulas can be modified to represent the true stress-strain curves. [16]

$$\sigma_T = \frac{P}{A} = \sigma(1 + \varepsilon) \tag{2-8}$$

$$\varepsilon_T = \ln(1 + \varepsilon) \tag{2-9}$$

The true stress-strain curves give a more correct description of intrinsic material strength, i.e. the values beyond yield.

The area under the curve up to the point of yield strength is referred to as the resilience. The area under the curve from yield to ultimate tensile is named toughness. This area shows the amount of energy that can be absorbed before failure. For good impact properties, the material should have good toughness properties. [16]

In this thesis the true stress-strain curves are used to quantify the tensile properties of the materials. As the equations (2-8) and (2-9) no longer apply after max load is reached, the stress and strain parameters need to defined. These important parameters are true yield stress (YS), true stress at max load (TS) and true strain at max load (Eu).

Dorward et al. rationalized in his study the effect of chemical composition of different Al-Mg-Si alloys on the strength and ductility. Also the toughness was examined and is related to intergranular (Ig) fracture tendencies. The toughness is negatively impacted by compositional and processing factors that promote Ig precipitations: excess silicon, low solutionizing temperatures, slack quench rates and low dispersoid (Cr/Mn) levels.

Peak strength is enhanced by 10-15 MPa for each 0.1% excess silicon, with a corresponding elongation decrease of 0.25%. For a given strength level, the highest elongation are achieved in excess silicon compositions. Lean (Mg0.78 wt% and Si 0.53wt%) and nominal (Mg0.93Wt% and Si 0.63 wt%) balanced chemistries have the best combination of strength and toughness. [17]

Another interesting study on the fracture mechanism was done by Vasudévan et al. The study concluded that intergranular fracture occurs in precipitation hardened aluminium alloys in the peak-aged and over-aged conditions and, to a smaller extent even in under-aged condition. The study also concluded that the phenomenon of macroscopic brittle fracture at Grain Boundary (Gb) which show microvoiding at Gb particles is an important fracture mechanism for precipitation hardened aluminium alloys. [18]

2.10 Three point bending test

The three point bending test is utilized to identify the bendability of the alloys. A flat plate is placed on two cylindrical bearings as a load is subjected by a punch in the middle of the sheet. An illustration of this type of bending test is shown in Figure 2-18.

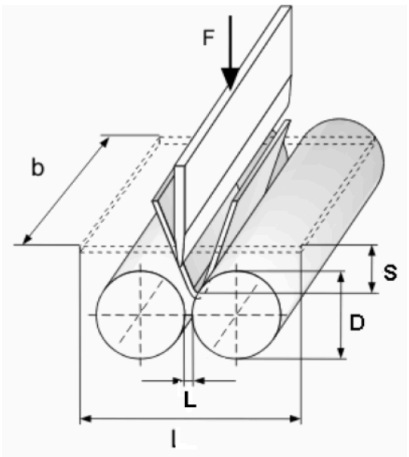

Figure 2-18: Illustration of the three point bending test. [19]

Figure 2-19: The moment M and Tension T in the bend. [20]

As the punch forces through the plate, a moment per unit width M and a tension per unit T width occurs in the bend area (Figure 2-19). The tension happens in the central axis (dotted lines). If the material outside the bend is not deforming, plane strain can be assumed. No strain parallel to the bend occurs. [20]

During bending, the area over the central axis compresses and the area under is under tension. At the same time the strain at the bend is proportional with the distance from the neutral axis. This implies that the strain under tension is greater than the strain in compression. [5]

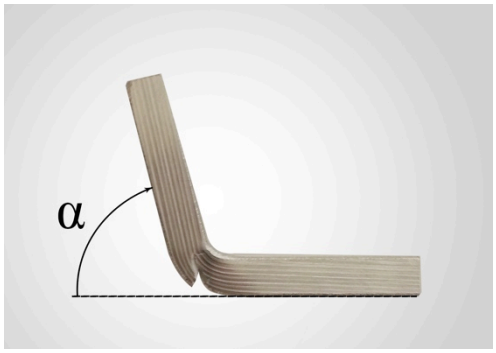

Figure 2-20: Definition of angle α.

To quantify the bendability of the material, the bending angle α is defined as shown in Figure 2-20. A large angle α at maximum force indicates high bendability. [19] In this thesis the angle is calculated at the crack initiation phase with the equation (2-10). The Figure 2-21 illustrates how the α angle is calculated. The measured extension at max load is used to determine the angle.

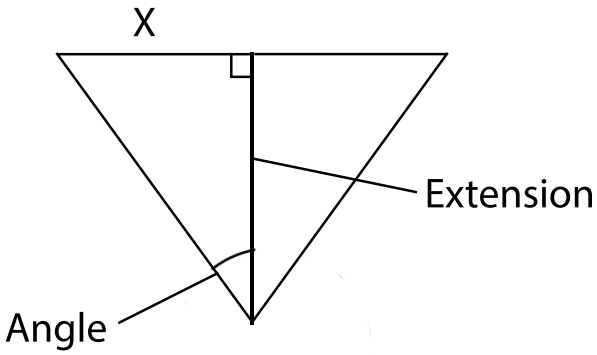

Figure 2-21: Illustration of the equation (2-9).

$$Bending\ angle\ \alpha = 180 - 2(\arctan\left(\frac{X}{Extension}\right)) \qquad \textbf{(2-10)}$$

As the bending angle is calculated based on the extension at maximum force, it gives an indication on the amount of energy absorbed before fracture occurs. In other words, the fracture mechanism is crucial to explain the measured bending angles. Sarkar et al. showed that small microcracks, initial surface roughness and hard particles aid the initiation of the shear bands. These then further lead to the initiation of fracture. [21]

3 Experimental

In this chapter, the different materials studied in this thesis are presented in detail. In addition all the characterization methods and test performed are described.

3.1 The Material

Three different Al-Mg-Si alloys were chosen in this thesis: C20-X1, C24-Y1 and C28-C2. The first alloy contains 0.537 wt% Mg and 0.515 wt% Si, almost a 1:1 ratio of the main alloying elements. The C24-Y1 has similar mounts of Si as the first alloy (0.571 wt%), only with more Mg (0.715 wt%). The last alloy contains more of both alloying elements: 0.83wt% Mg and 0.75 wt% Si. As for rest of the elements amount remain similar for the three alloys, except for Mn and Cr. The chemical composition is given in Table 3-2.

Table 3-1: Chemical composition of the different aluminium alloys. The amount of each alloying element is given in [wt%].

Cast #	Alloy	Mg	Si	Fe	Cu	Mn	Cr	Ti
71574	C20-Y1	0.537	0.515	0.209	0.014	0.137	0.003	0.094
71614	C24-X1	0.712	0.571	0.193	0.183	0.551	0.157	0.017
71679	C28-C2	0.83	0.75	0.20	0.23	0.55	0.16	0.02

The aluminium alloys are studied in three different tempers: T6, T7 and W/T4. The T6 alloys were age hardened at 185 °C for 6 hours and T7 alloys were age hardened at 205 °C for 2 hours. The W/T4 were delivered “as extruded” and reheated at 540 °C for 20 min and quenched in water.

Table 3-2: The alloys and tempers of each profiles.

	Heat treatment			
Alloy	Flat Profiles			Box Profiles
C20-Y1	C20-Y1 T6	C20-Y1 T7	C20-Y1 W/T4	V7-S0 T6
C24-X1	C24-X1 T6	C24-X1 T7	C24-X1 W/T4	V13-S0 T6
C28-C2	C28-C2 T6	C28-C2 T7	C28-C2 W/T4	-

All three alloys were delivered as extruded flat profiles. The C20-Y1 and C24-X1 alloys were also presented as 2-chamber box profiles. To avoid any confusion, the C20-Y1 box profile

will be referred to as V7-S0 and the C24-X1 box profile as V13-S0. This notation is taken from the project M4 by S.Dumolin et al. [2]

The flat profiles are studied in the T6, T7 and W/T4 temper and box profiles in T6 temper. The materials matrix is summarized in Table 3-2.

The flat profiles have a thickness of 6 mm and a width of 10 mm. The sidewalls of the box profiles were cut out to width of approximately 50mm, with a thickness of 2,6 mm. Only the sidewalls of the box profiles were studied in this paper. The dimensions and geometry of the profiles are given in Figure 3-1 and Figure 3-2.

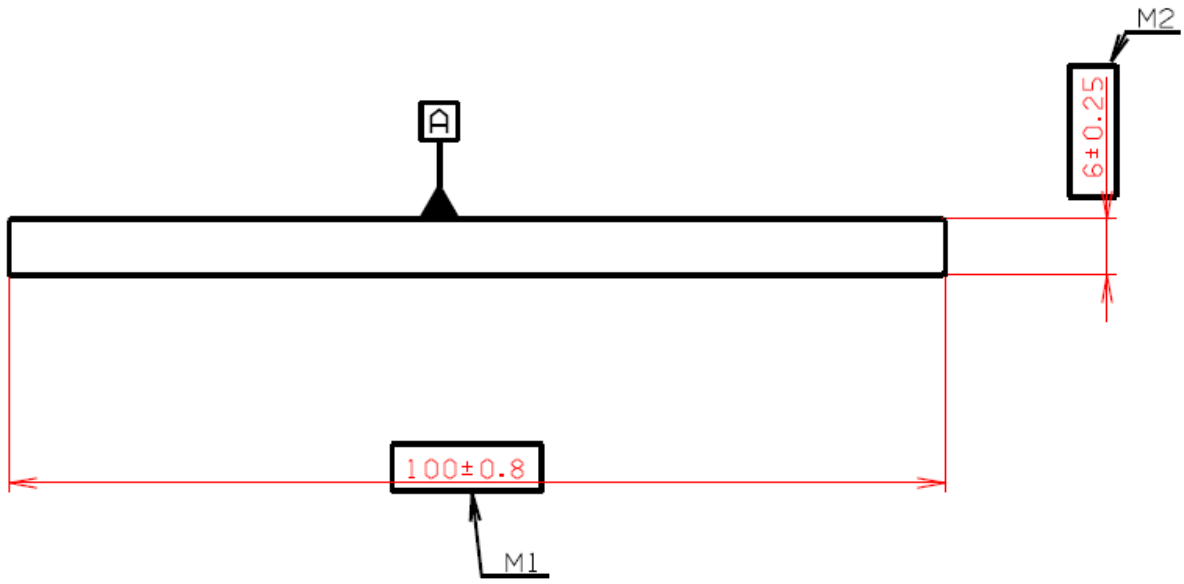

Figure 3-1: The shape of the flat profiles. All dimensions are given in millimetres.

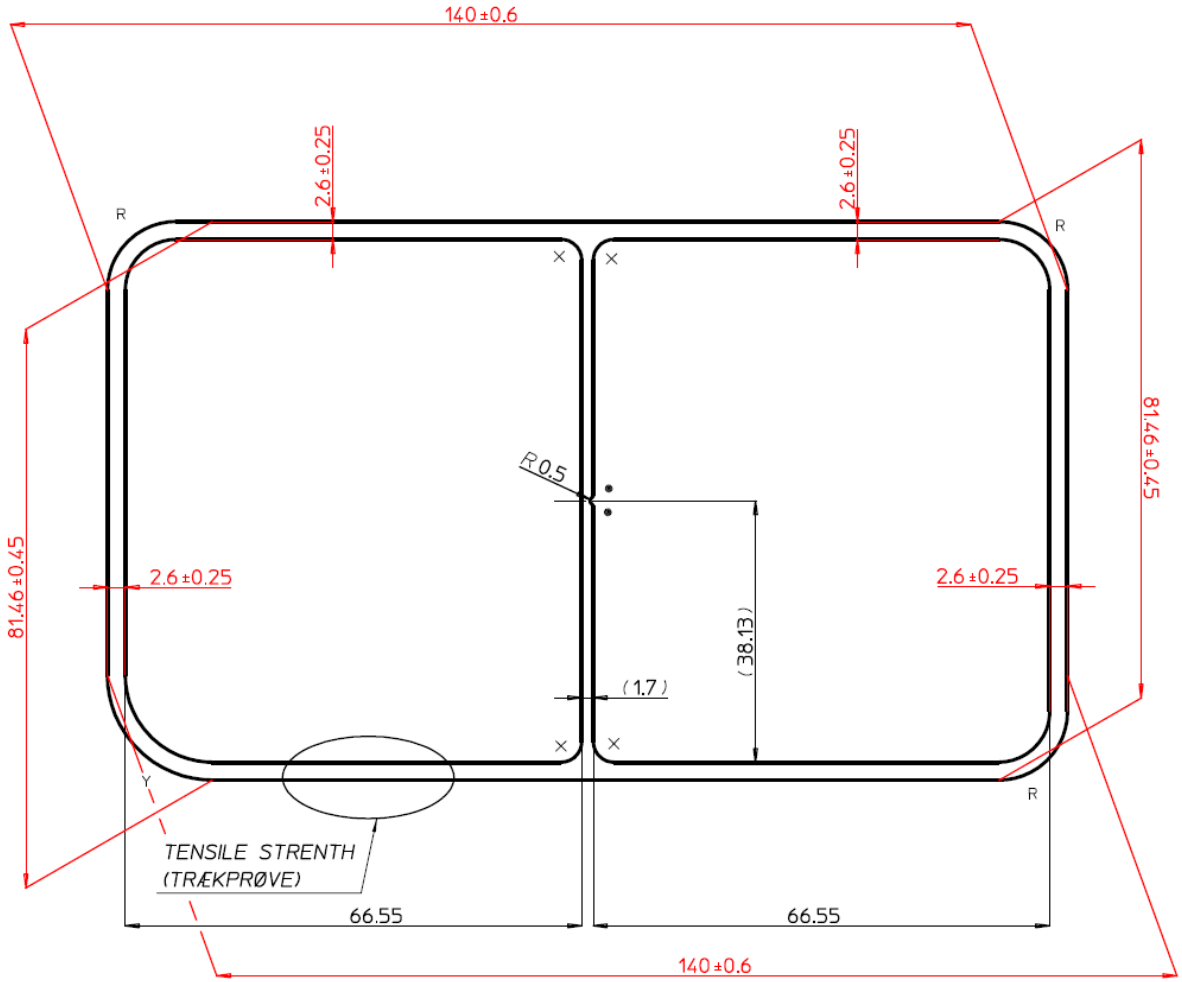

Figure 3-2: The shape and dimensions of the box profiles. All dimensions are given in millimetres.

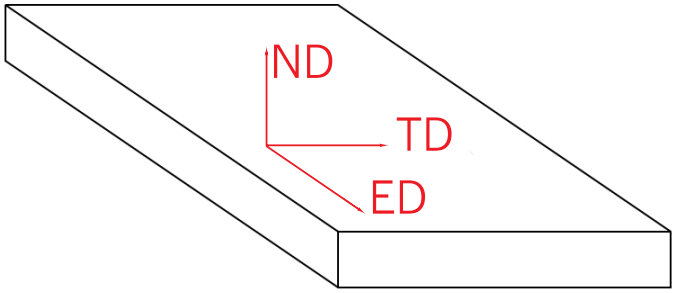

Figure 3-3: Definition of the directions of the extruded profiles.

As aluminium billets get extruded the microstructure is affected, and is heavily direction dependent. An illustration of the different directions is given in the Figure 3-3.

3.2 Characterization by Light Optical Microscopy (LOM)

Small samples were cut from the profiles and the plates. The samples were first grinded with sandpaper, and were then polished. The grinding sequence started with 80 SiC paper to 2400 SiC paper on a Stuers Rato Force 4 grinding machine. Each step lasted 30 seconds. Then the Stures Tegra was used for the polishing. The sequence started with 9μm, 3μm and 1μm for 2 min each. The samples were then anodised for 90s in 5% HBF4, with a potential of 20 V.

The prepared samples were then placed in a Leica MEF4M microscope with a polarizator and a sub-parallel λ-filter.

3.3 EBSD characterization

The profiles were studied with EBSD method. Grinding and polishing similar to procedure described for LOM characterization, was done down to 1μm polishing.

Mechanical polishing leaves a thin layer of deformation, which has to be removed by electro polishing. This process is done with Struers LectroPol-5, with an A2 electrolyte. The content of the electrolyte is given in Table 3-3. First the electrolyte was cooled to a temperature of -30C. When the right temperature was reached, the electrolyte was squirted against the sample's surface. This was done with a potential of 20 V for 16 seconds. Finally the samples placed in Fischone plasma cleaner for the duration of 3 min.

Table 3-3: Content of the A2 electrolyte.

Percloric acid	78ml
Water	120ml
Ethanol	700ml
Butylcellosolve	100ml

The EBSD analysis was preformed in Zeiss Ultra 55 LE FESEM, with an EBSD detector. The parameters used for this process is given in the Table 3-4.

Table 3-4: The configuration used for EBSD method.

Aperture	300 µm
Signal	Backscatter Electrons
High Current Mode	On
EHT	20 kV
Working Distance	20- 24 mm
Tilt angle	70°

Samples were prepared for the scans of the microstructure in middle of the ED-ND cross-section. A set of samples was also prepared to characterize the crystallographic texture of the surface layer, as seen in Figure 3-4. To analyse the texture in the surface layer, the ED-TD cross-section of the samples was grinded, polished and electro-polished within the surface layer.

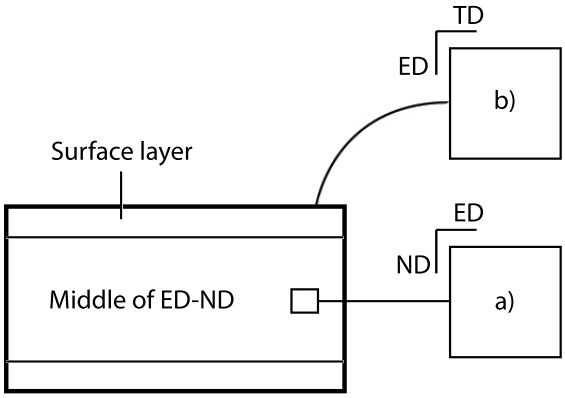

Figure 3-4: The samples prepared for EBSD: a) middle of ED-ND cross-section and b) the surface layer.

The NORDIFF software was used to collect the diffraction patterns, and the TSL OIM software was used the index the patterns.

3.4 Particle characterization

The Z-contrast method was used the on SEM. Similar to the preparation procedure for the EBSD method the samples were manually polished and electro polished. Again, ED-ND cross-section of the profiles was studied. The configuration of the SEM for Z-contrast method is summarized in table 3-4.

Table 3-5: Particles analysis configuration of the SEM.

Aperture	120 µm
Signal	Backscatter Electrons
High Current Mode	On
EHT	15 kV
Working Distance	10 mm

The images were processed in ImageJ 1.48 software. By adjusting the brightness and contrast of the pictures obtained in the SEM, so that the primary particles are clearly distinguishable from the surrounding matrix the software identify the size and shape of the particles. The software then outputs wanted values: number of particles, size and particle per cent area fraction.

3.5 Tensile test

To produce stress-strain curves for the materials at W/T4 temper, tensile test were performed. After being cut to the desired dimensions, the specimens were heated to 540 for 20 minutes, and then quenched in water to achieve the W temper. The material was heat treated and quenched within 24 hours of the test was performed.

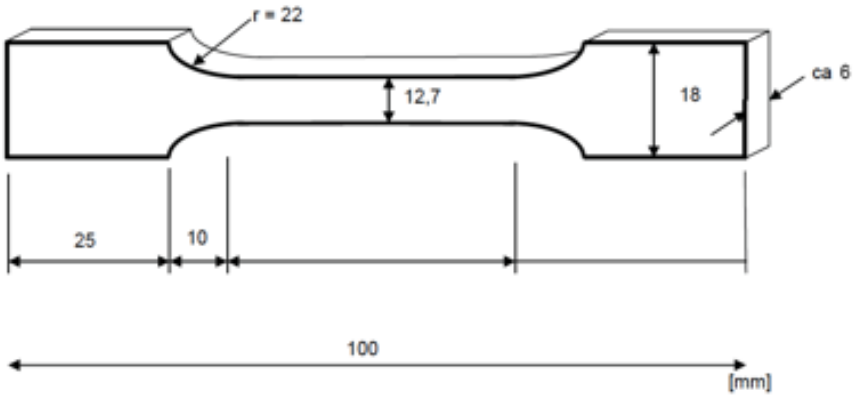

Figure 3-5: Dimensions of the tensile specimens.

The dimensions of the tensile sample are shown in Figure 3-5. No reduction of the thickness was done to the starting profiles, making the tensile specimens 6 mm thick. The overall length of the samples was 100 mm.

A 100kN load cell was used with a 25 mm extensometer. The tensile velocity was set to 2mm/min.

The specimens were cut in 0°, 45° and 90° in relation to the extrusion direction. Due to a lack of material only two parallels in the 45-orientation were produced, while three parallels were created for the 0 and 90 orientations.

3.6 Bending test

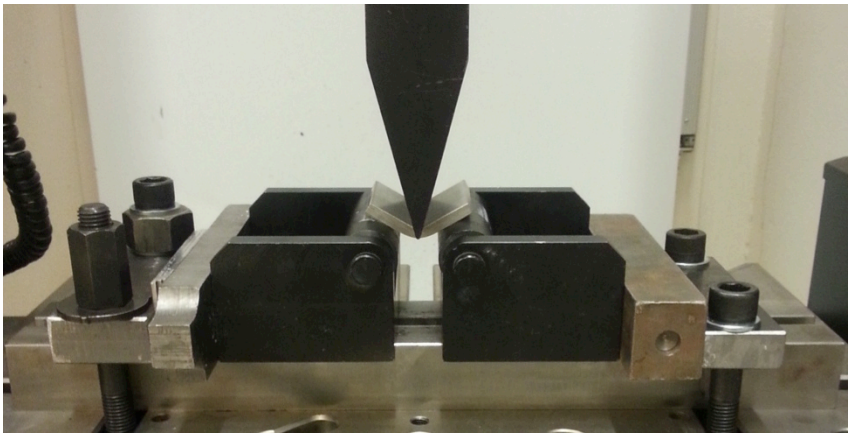

Figure 3-6: The bending test setup.

A three point bending test was performed for the different materials. Square samples were cut from the profiles to the dimension of 60x60mm and 50x50mm as shown in Table 3-6. The T4/W materials were heat treated the day before the test was performed.

Table 3-6: Dimensions of the bending test samples. The thickness of the flat profiles were 6mm and the thickness of the box profiles were 2,6 mm.

	W/T4	T6	T7		T6
C20-Y1 C24-X1 C28-C2	60x60mm	60x60mm	50x50mm	V7 V13	50x50mm

Figure 3-6 shows the actual setup of the bending test. The samples were placed on two cylindrical bearings. As a force is applied through the punch the samples bends in the middle. The bearings are free to rotate as sample bends. The tests were stopped manually when no more bending occurred. The distance between the cylindrical bearings was to 20 mm and with a punch nose radius of 1,25 mm. The test velocity was set to 20mm/min. The test was done at NTNU with an Instron bending system.

The maximum force registered of each the bending test was registered as well as the corresponding vertical extension. From these values the bending angle of each sample was calculated with Equation (2-10).

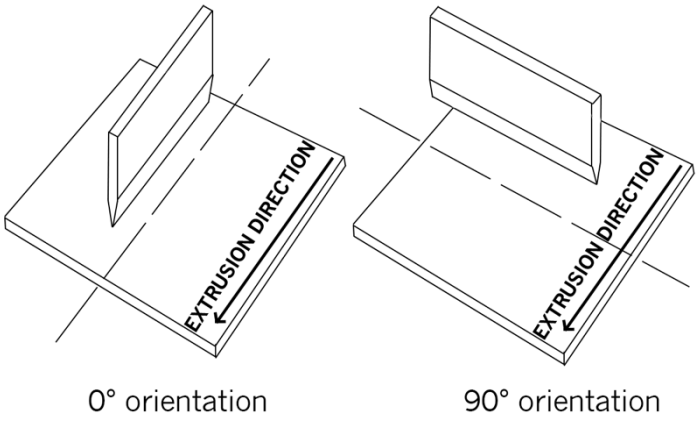

Figure 3-7: The definition of the orientations of the bending test. (VDA)

The bending tests were performed in 0- and 90-orientations in respect to the extrusion direction. Figure 3-7 shows how the two orientations are defined. Three parallels of each material at their specific temper and orientations were tested, making a total of 66 samples.

4 Results

The results of the performed experiments are presented in this section in the form of diagrams, tables and figures. The characterization of the microstructure is presented first, followed by mechanical properties of the material. The microstructure of the material is characterized by LOM, SEM and EBSD. The texture of the material is also represented by EBSD, in form of pole figures and ODFs. Characterization of the primary particles are done by the Z-contrast method in SEM. Mechanical testing includes stress strain curves and the bending angle as obtained by a three point bending test.

4.1 Heat treatment of materials delivered "as extruded"

The material delivered in the as extruded state, are reheated at 540° C and quenched to achieve the W/T4 temper. The objective was to see to which extent and how a re-solution heat treatment of this kind affected the as extruded microstructure of C24-X1 material and hardness. The effect of the heat treatment is studied by microstructure characterization and hardness measurements. In Figure 4-1 the as extruded C24-X1 alloy is characterized before heat-treatment and Figure 4-2 shows the effect of the heat-treatment on same alloy. Both the characterization of the microstructure and hardness measurements is done within 24 hours of the heat treatment (i.e. in a T4 condition).

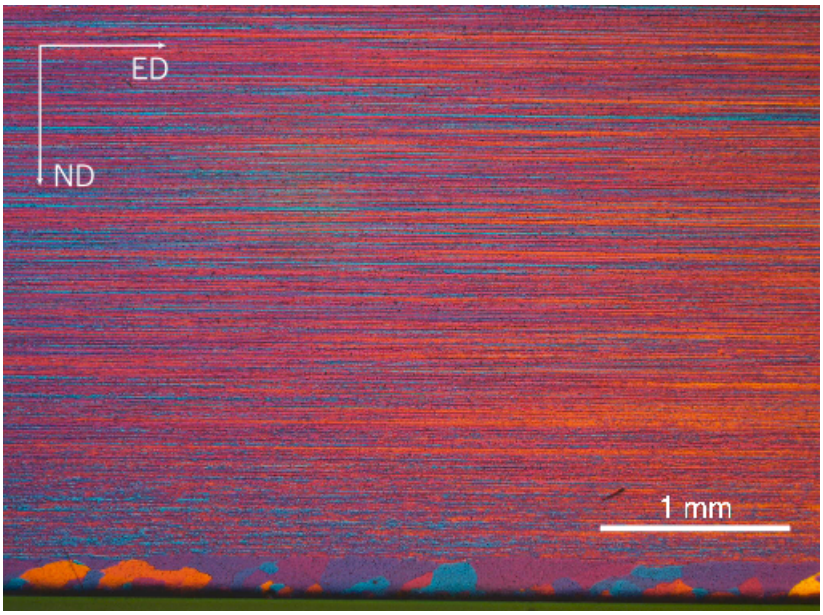

Figure 4-1: Microstructure of C24 delivered as extruded ED-ND cross section.

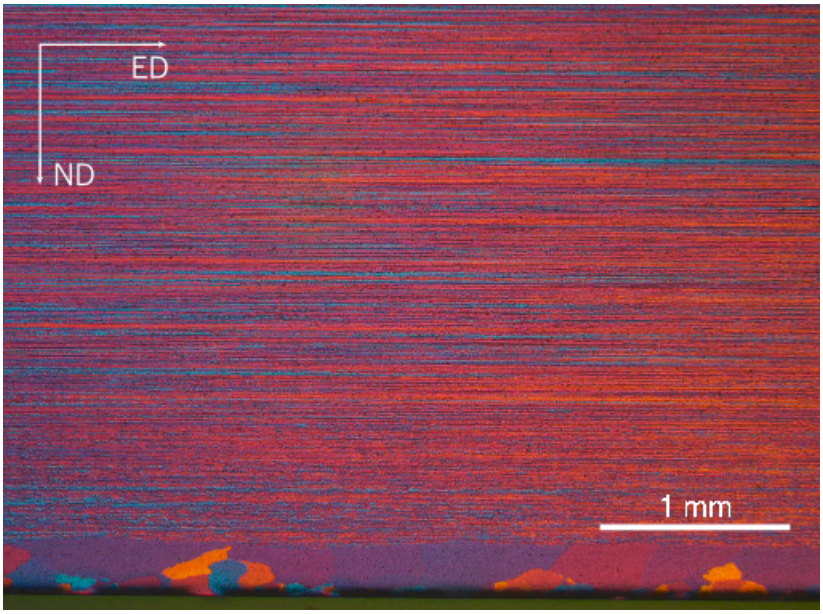

Figure 4-2: C24 delivered as extruded, heat treated for 20 min at 540° C and quenched.

The micrographs of the microstructure before and after heat treatment of the material show little differences. The recrystallized layer is seen to be only slightly larger after heat treatment, i.e. such heat treatment does not "destroy" the fibrous microstructure of the as extruded state.

Table 4-1: The difference of measured hardness before and after heat treatment of C24 "as extruded" and naturally aged for about a year.

Time	Average Hardness	SD
[min]	[HV]	[HV]
0	79,26	4,0
20	62,4	3,0

Table 4-2: The difference of measured hardness before and after heat treatment of C24 T6.

Time	Average Hardness	SD
[min]	[HV]	[HV]
0	100,5	4,6
20	66,0	2,4

After 20 minutes at 540° C, both the C24-X1 "as extruded" and C24-X1 T6 experience a significant loss in hardness, i.e. in a condition that can be characterized as a T4-temper

condition (i.e. solution heat treated and naturally aged) as the hardness is not measured directly after quenching but after some hours at room temperature (< 24 hours). The former display a hardness of 62,4 HV and the latter 66,0 HV. In other words, regardless of the starting state of the materials a similar strength is reached. The initial hardness of the "as extruded" is the result of one year of natural ageing of this material.

4.2 LOM Characterization

The three alloys in T6-temper are characterized by light microscopy in Figure 4-3 to Figure 4-5. The C20-Y1 alloy displays a recrystallized microstructure. The grain size is seen to vary throughout thickness in the ED-ND cross-section. At the surface, very small grains are seen while just below much coarser grains are observed. The light intensity of the grains is seen to be stronger close to the surface.

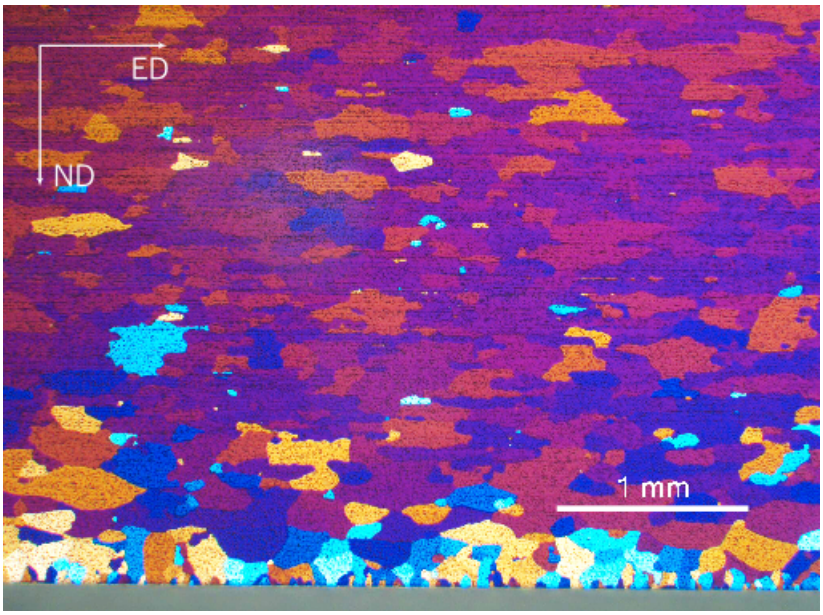

Figure 4-3: The ED-ND cross-section of the C20-Y1 T6 alloy

The characterization of the two other alloys shows a fibrous structure with elongated grains parallel to the extrusion direction, with a recrystallized layer at the surface of the ED-ND cross-section. Figure 4-4 displays the microstructure of the C24-X1 alloy and Figure 4-5 the microstructure of C28-C2. The recrystallized layer is measured to be approximately 300 µm for C24-X1 and about 100 µm for the C28-C2 alloy.

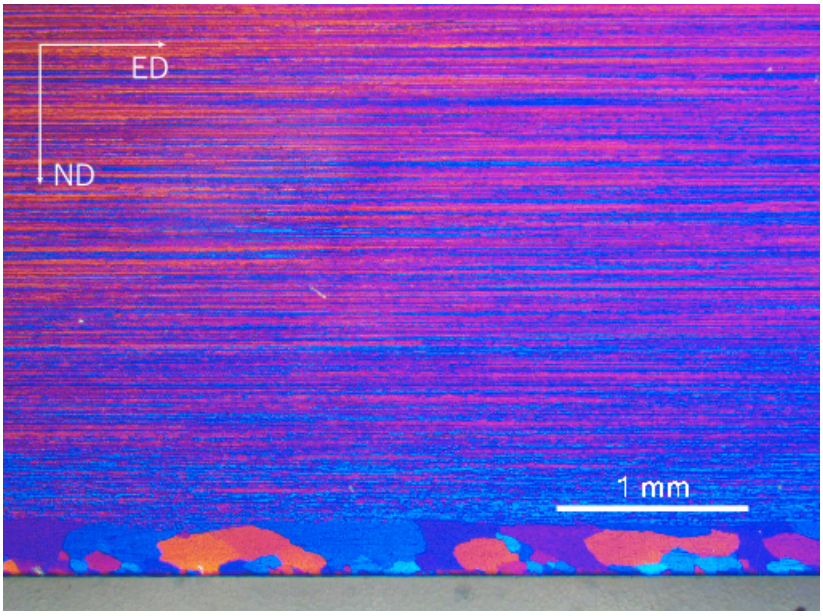

Figure 4-4: The ED-ND cross-section of the C24-X1 T6 alloy.

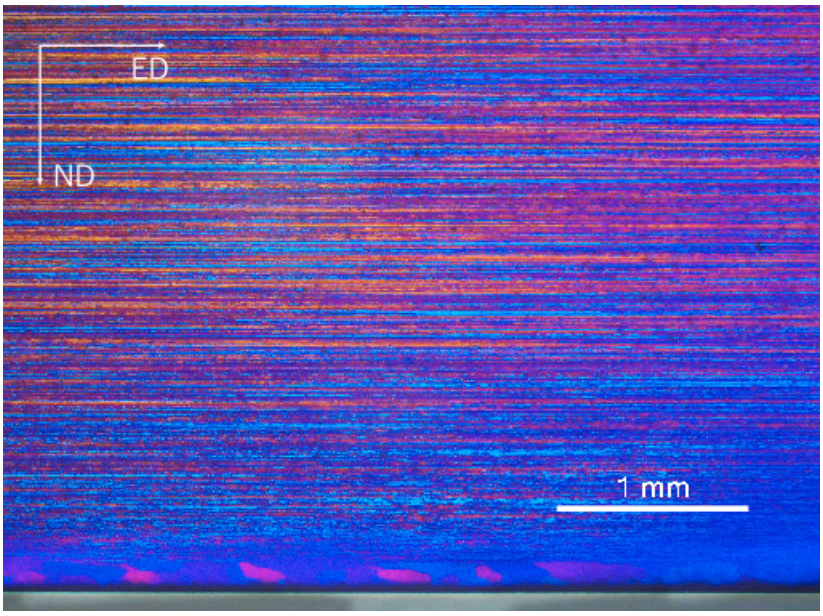

Figure 4-5: The ED-ND cross-section of the C28-C2 T6 alloy.

4.3 EBSD characterization

The results from the EBSD characterization are presented here, which include microstructure scans, pole figures and Orientation Distribution Functions (ODF).

4.3.1 Microstructure

EBSD characterization is performed to study the microstructure in the ED-ND cross-section at a higher magnitude. The EBSD scans are also used for the characterization of texture. First the scans of the microstructure are presented. Further on the texture is depicted by pole figures and ODFs. The recorded average CI of the different scans is shown in Table 4-3.

Table 4-3: Recorded CI index of EBSD scans.

Placement	Average CI
C20-Y1 middle of ED-ND	0.82
C20-Y1 surface layer	0.89
C24-X1 middle of ED-ND	0.69
C24-X1 surface layer	0.88
C28-C2 middle of ED-ND	0.56
C28-C2 surface layer	0.85

The results are shown in Figure 4-6 for a) C20-Y1 T6, b) C24-X1 T6 and c) C28-Y1 T6. The scanned area is the middle of the ED-ND thickness, as explained in the experimental section 3.3. The inverse pole figure and the orientation of the materials are included in the Figure 4-6. It should be mentioned that the two fibrous alloys are not completely parallel with the extrusion direction. The elongated grains are seen to be slightly rotated, due to experimental difficulties to align the specimens exactly.

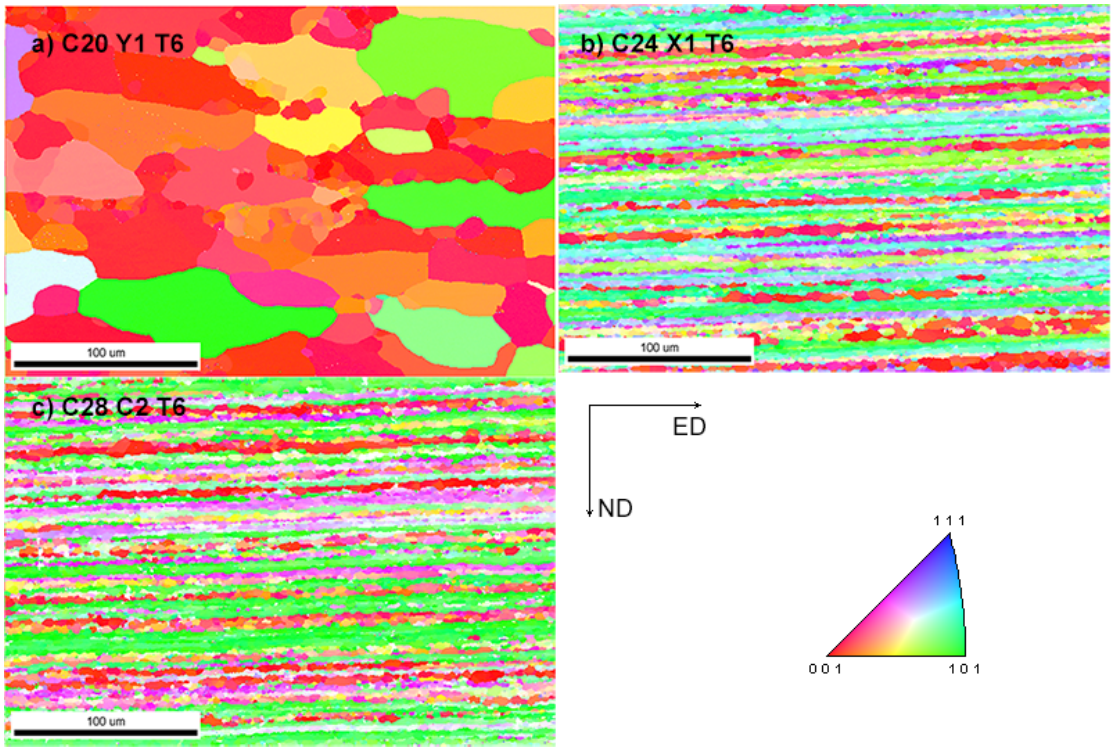

Figure 4-6: EBSD characterization of the middle surface.

The recrystallized C20-Y1 alloy shows a combination of large and small equiaxed grains. The alloy is dominated by grains oriented in the 001-direction, as seen by the red colour in the included inverse pole figure.

The two alloys C24-X1 and C28-Y1 contain much smaller flattened grains, i.e. a typical subgrain microstructure. This is consistent with the un-recrystallized fibrous structure also observed by LOM in Figure 4-4 and Figure 4-5. Both materials are seen to contain a large amount of grains oriented in the 101-direction and some in the 001-direction, illustrated by the dominating green and red colours

4.3.2 Texture - Pole figures

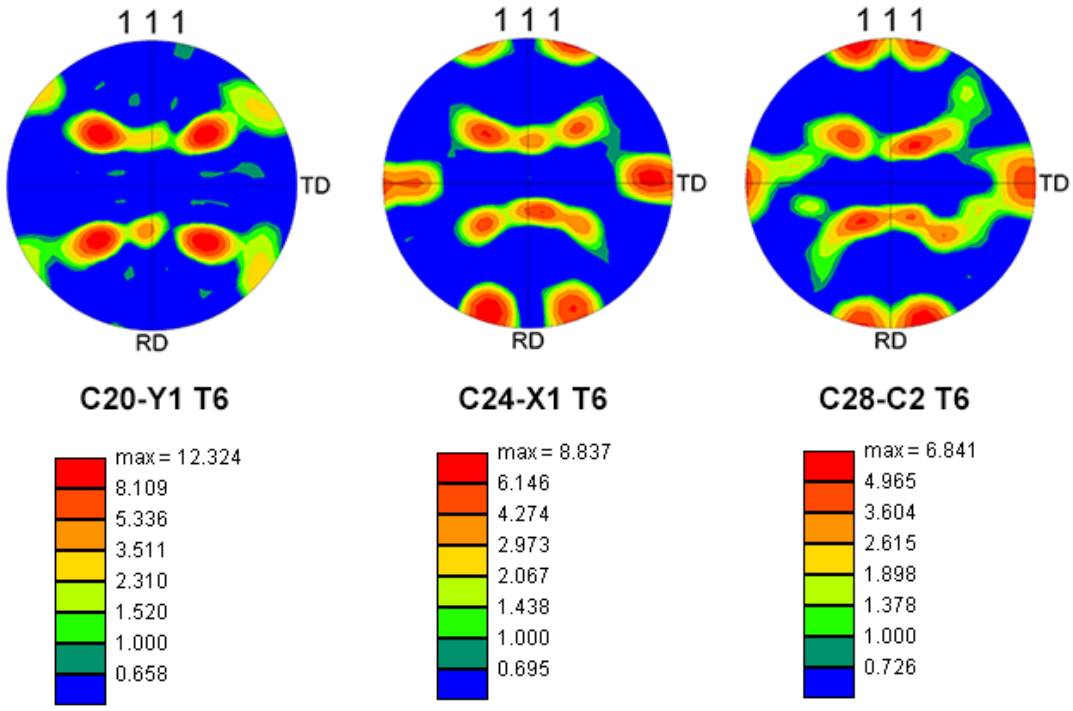

Figure 4-7: Pole figures of the middle of the ED-ND cross-section.

The texture of the materials presented in this section is obtained by EBSD method. The 111 pole figures shown in Figure 4-7, are linked to the scans of the microstructure in Figure 4-6. The pole figures are presented with the their respective orientation distribution intensity.

The pole figure of the C20-Y1 alloy shows a strong cube texture. The C24-X1 and the C28-Y1 alloy have more typical deformation texture characteristics consistent with their fibrous non-recrystallized grains structure. The distribution intensity of the C20-Y1 pole figure is highest, indicating a strong texture. As seen in Figure 4-6 a) the dominating red colour of the grains gives a strong texture. The C24-X1 pole figure shows a weaker texture than C20-Y1, but the texture is still well defined. The weakest texture is seen for C28-C2.

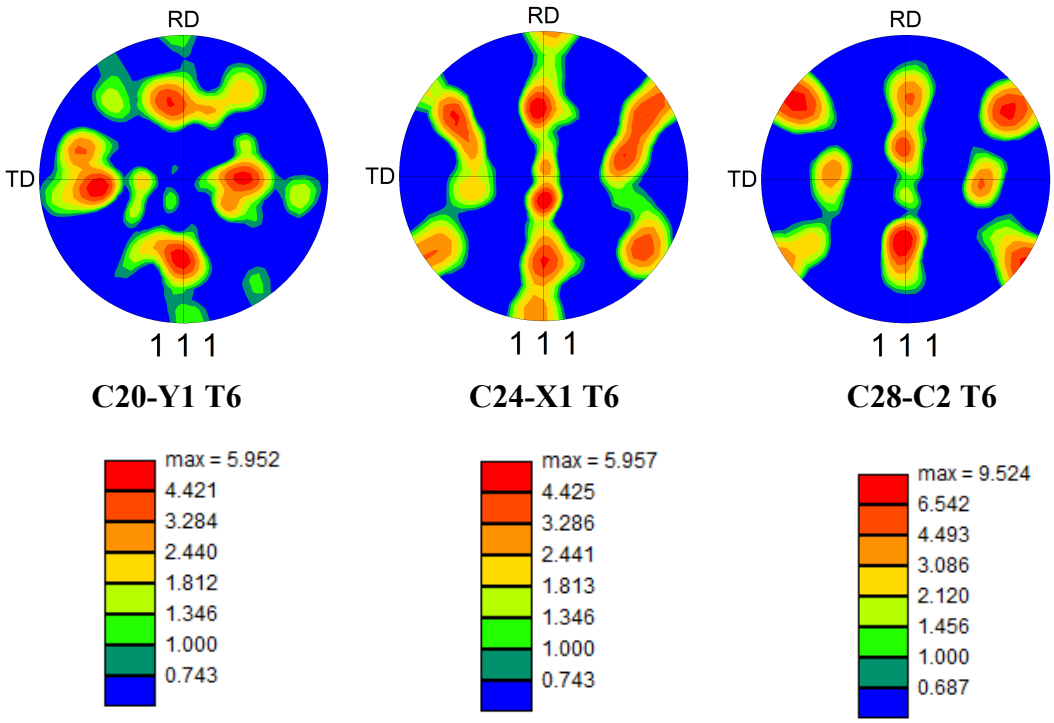

Figure 4-8: Pole figures of the crystallographic texture in the surface layer.

In Figure 4-8 the texture in the surface layer is presented. As explained in the experimental section 3.3, these pole figures are obtained by examining the ED-TD cross-section. The microstructure scans are shown Appendix A. The microstructure of the ED-TD cross-section showed a recrystallized microstructure for the fibrous alloys from which these textures are obtained, which confirms that the pole figures are taken from the recrystallized surface layer.

The 111 pole figures of the surface layer are given in Figure 4-8. It is often difficult to define the exact texture components present from the pole figures above. Pole figures often only give a qualitative picture and examples of typical textures, composed of a set of individual components are needed to identify the difficult texture components. Alternatively the ODFs are often used to identify the texture components as they often are more informative and easier to analyse.

Examples of typical ODFs of wrought aluminium products presented in theoretical background section (section 2.6) are used as reference for interpretation of the recalculated ODFs obtained here.

4.3.3 ODF - C20-Y1

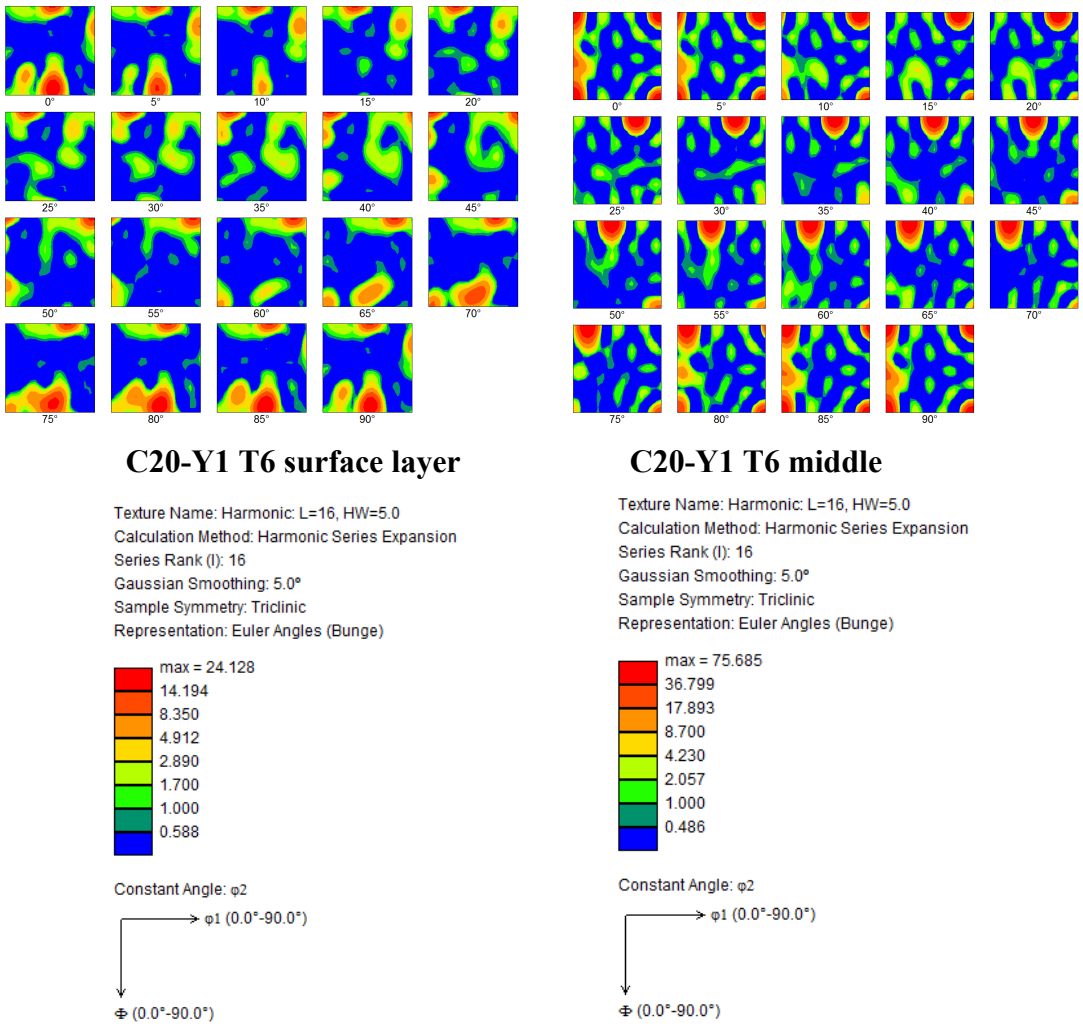

Figure 4-9: ODF of the surface layer and middle of the ED-ND cross-section of C20-Y1 T6.

First the ODF of the surface layer is considered, seen to the left in Figure 4-9. For the first square i.e. corresponding to $\phi_2 = 0$, a strong texture component is seen in $\phi_1 = 45$ and $\Phi = 0$ and 90. This dominant component is again noticed in the $\phi_2 = 45$ section, in the two top corners: $\Phi = 0$ at $\phi_1 = 0$ and 90. This texture component is indicated in the theoretical background section in Figure 2-15, and is referred to as {001}<110> Rotated Cube.

For the scans in the middle of the cross-section, the cube texture component is seen in the four corners of $\phi_2 = 0$. This is consistent with the C20-Y1 111-pole figure in Figure 4-7. The {001}<100> Cube component is also noticed in the $\phi_2 = 45$ section, at $\phi_1 = 45$ and $\Phi = 0$.

4.3.4 ODF - C24-X1

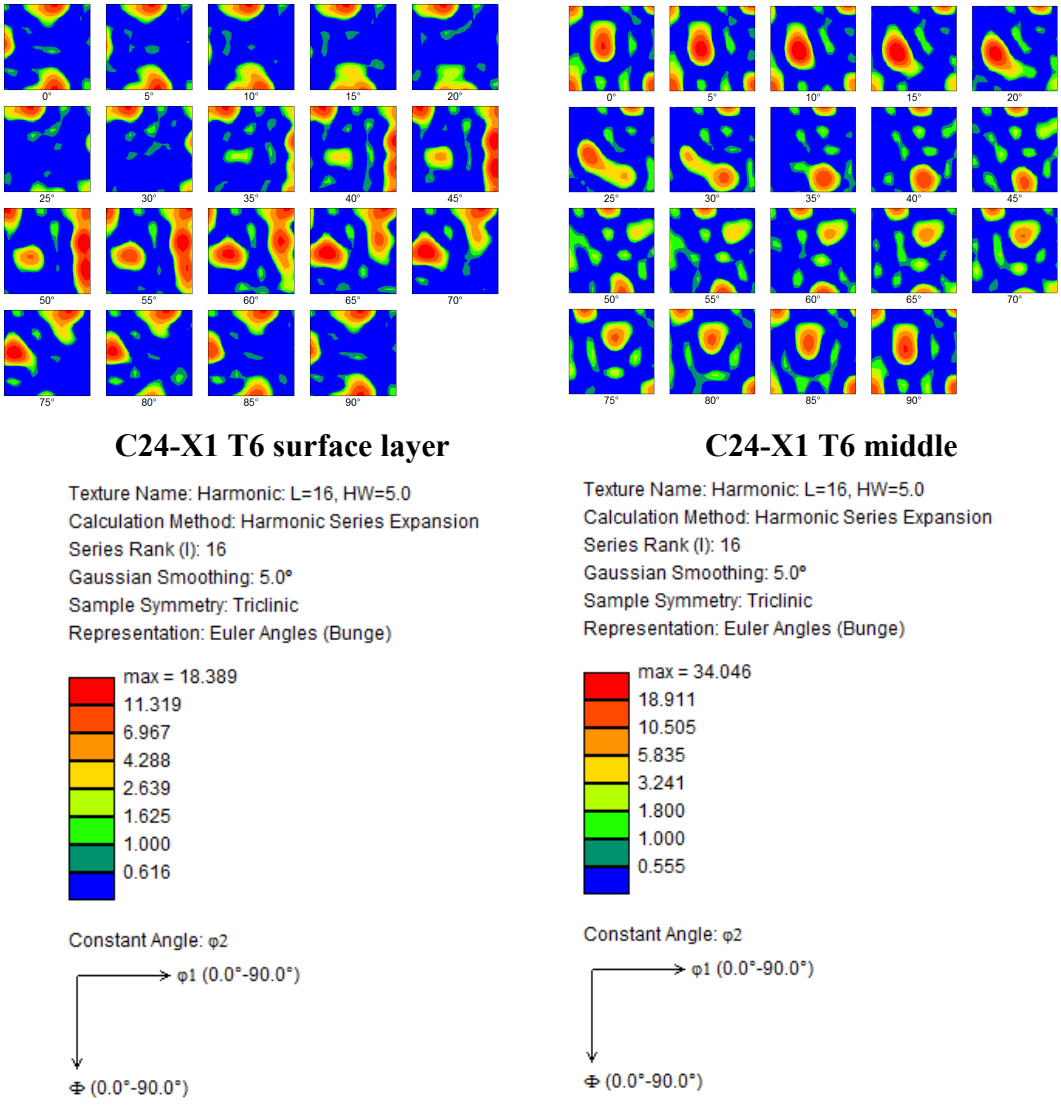

Figure 4-10: ODF of the surface layer and middle of the ED-ND cross-section of C24-X1 T6.

In Figure 4-10 the recalculated ODF from the surface layer is seen to the right, and to the left the ODF of the middle of the ED-ND cross-section. The top surface layer, which contains recrystallized grains are seen to have a {001}<110> Rotated Cube texture. In addition the presence of a {011}<100> Goss-texture is clear. This component is seen in the $\phi_2 = 0$ section, at $\phi_1 = 0$ and $\Phi = 45$.

The scan performed on the fibrous microstructure in the profile mid-section, shows a combination of strong {011}<112> Brass component and a {001}<100> Cube component. The combination of these components makes up the so-called deformation texture, typical for heavily plain strain deformed aluminium alloys

4.3.5 ODF - C28-C2

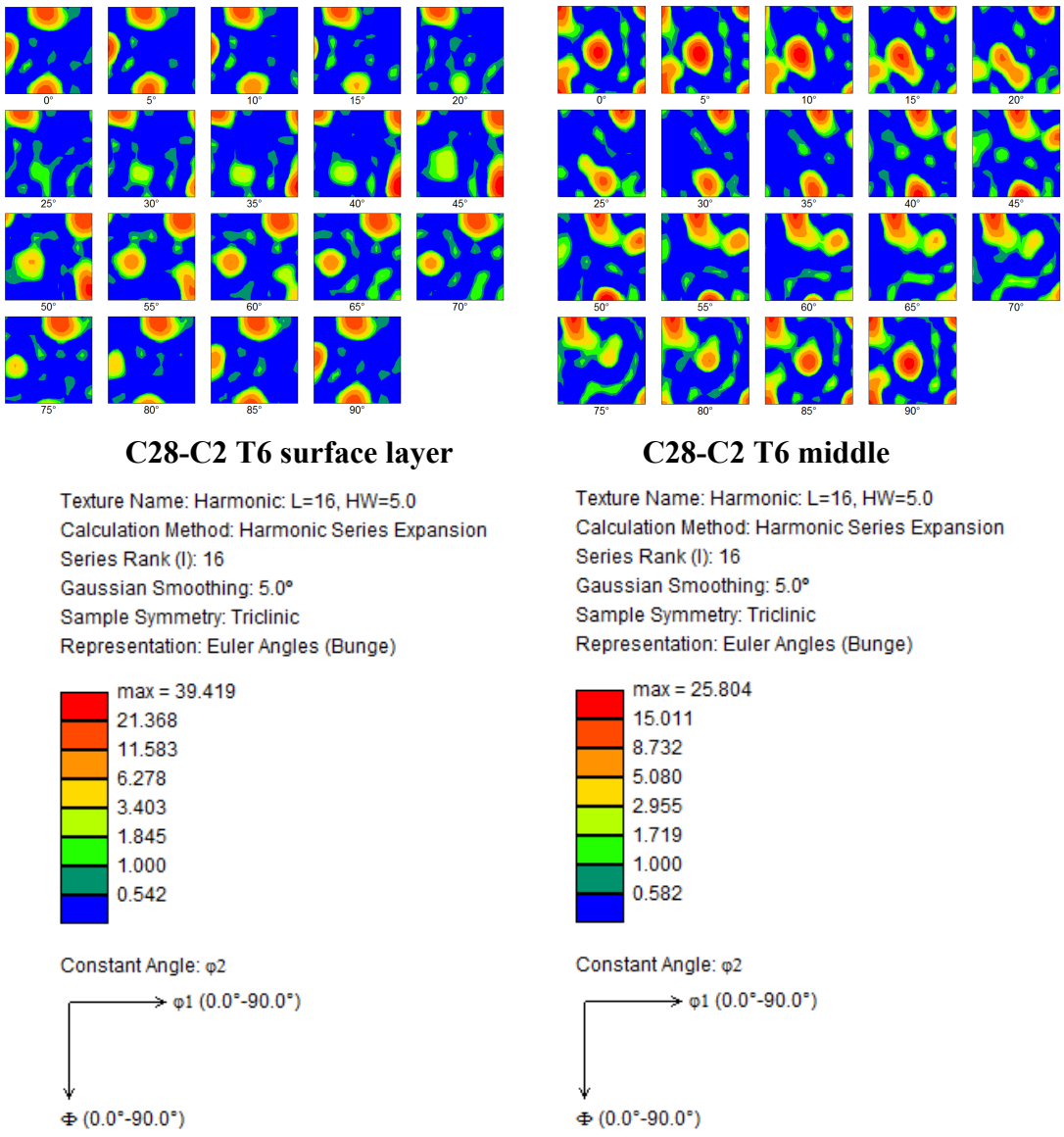

Figure 4-11: ODF of the surface layer and middle of the ED-ND cross-section of C28-C2 T6.

The texture seen in the ODFs of the C28-C2 T6 is similar to the C24-X1 T6 alloy. It should pointed out that these are not identical, but the main features are comparable. In the surface layer of C28-C2 profile, {001}<110> Rotated Cube and {011}<100> Goss are the dominant components. In the middle of the cross-section the {001}<100> Cube and {011}<112> Brass texture are seen to be the most important components.

4.4 Particle Characterization

The primary particle structure of C20-Y1, C24-X1 and C28-C2 is studied by Z-contrast in SEM. Figure 4-12 to Figure 4-14 show the ED-ND cross-section of the different materials. To insure a representative particle distribution, two SEM scans were performed at 500x and 2000x magnitude. The average size and area fraction of the particles are given for the scans at both magnitudes.

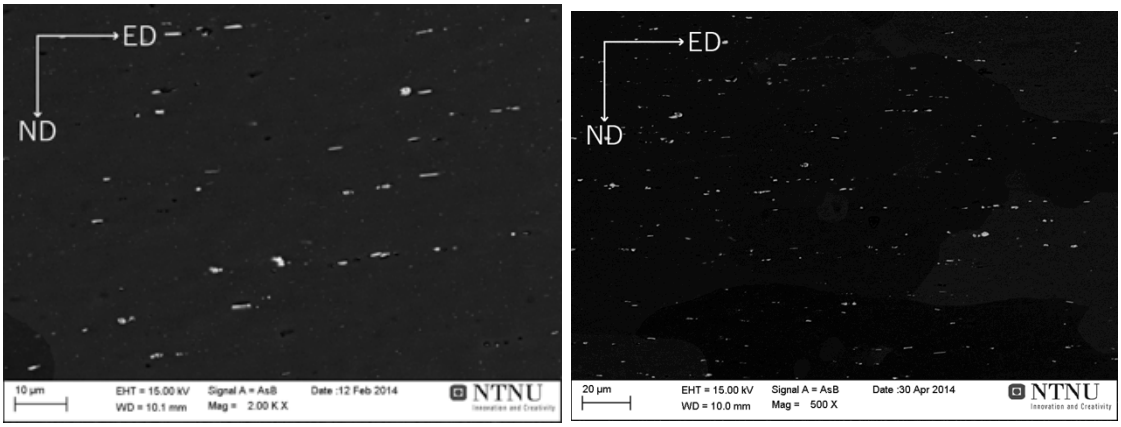

Figure 4-12: SEM characterization of the particles in C20-Y1 T6 alloy: to the left 2000x magnitude, and to the right 500x magnitude.

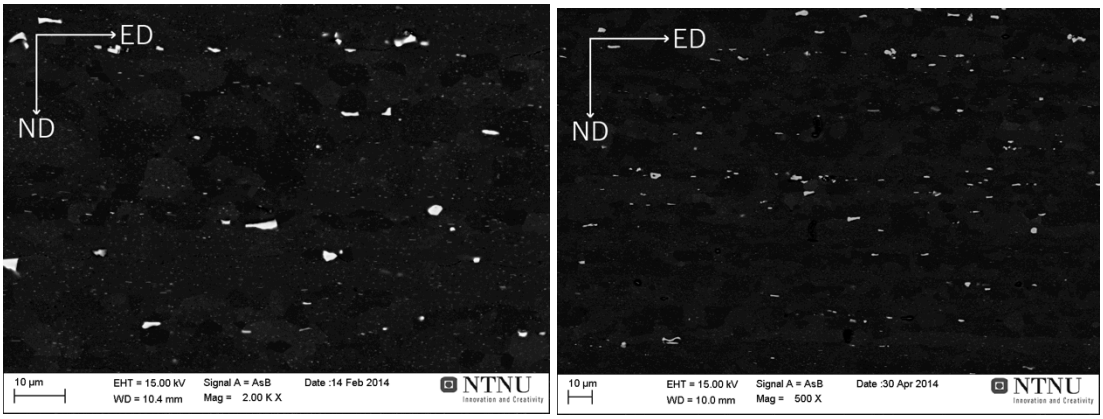

Figure 4-13: SEM characterization of the particles in the C24-X1 T6 alloy: to the left 2000x magnitude, and to the right 500x magnitude.

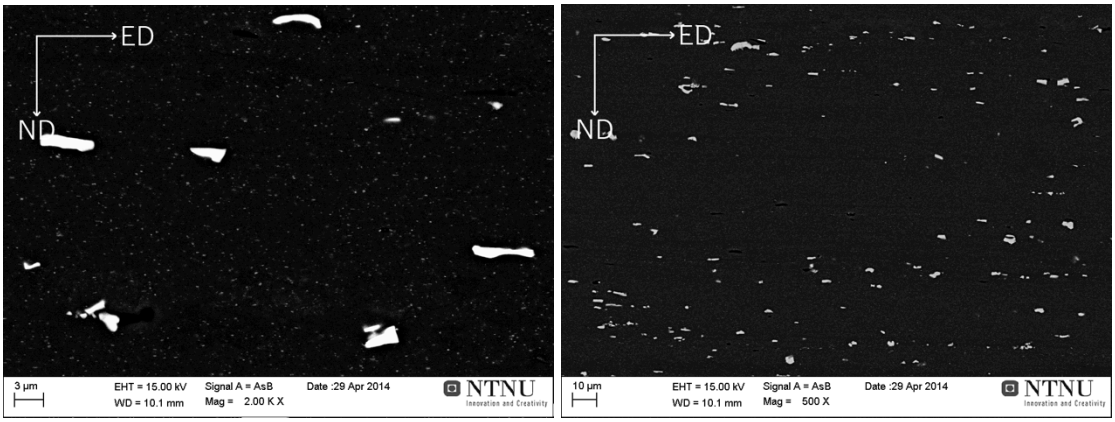

Figure 4-14: SEM characterization of the particles in the C28-C2 T6 alloy: : to the left 2000x magnitude, and to the right 500x magnitude.

Table 4-4: Calculated particle size, area fraction and number of particles.

Alloy	Mag	Number	Total Area	Average Size	%Area
C20-Y1 T6	2000x	58	41.028	0.707	0.515
C20-Y1 T6	500x	293	180.477	0.616	0.525
C24-X1 T6	2000x	47	49.414	1.051	0.644
C24-X1 T6	500x	241	229.720	0.953	0.670
C28-C2 T6	2000x	19	29.926	1.575	1.276
C28-C2 T6	500x	308	478.048	1.552	1.307

The area fractions of particles are given in the Table 4-4. For each alloy, the scans performed at 500x and 2000x magnitude shows similar particles percent area fraction. The particles cover slightly more of the area of the C24-X1 compared the C20-Y1 alloy. The C28-C2 alloy is seen to have an area fraction of primary particles between 1.28-1.30%, which is approximately the double of the two other alloys.

The average particles size is seen to be lowest in C20-Y1, and the largest in C28-C2 with the C24-X1 lying in between. For all alloys, the particles are seen to be elongated parallel with ED.

4.5 Stress-Strain Curves

With the exception of the T4-temper, true stress-strain curves presented in the section were provided by Svein Skjærvold (SAPA), i.e. the tensile test were not performed by the author of this thesis.

The true stress-strain curves are presented in three major parts. First the three alloys are compared at a specific temper. Then the flow curves at the different tempers are plotted against each other for each given alloy. Finally the anisotropy, in terms of performance in the different orientations relative to the extrusion direction, of the materials is considered. The presentation of the results are structured in this way to consider and compare the properties in the different tempers, alloys and orientations in an informative manner. Hopefully this structure allows for a clearer examination of the properties.

Table 4-5: The important values of the tensile tests.

	True Yield Stress (YS) [MPa]			True stress at max load (TS) [MPa]			True Strain at max load (Eu)		
Orientations	0°	45°	90°	0°	45°	90°	0°	45°	90°
C20-Y1 T4	96	89	95	207	250	219	0,12	0,31	0,25
C24-X1 T4	124	114	123	290	271	291	0,18	0,24	0,22
C28-C2 T4	157	140	155	352	321	350	0,18	0,23	0,21
C20-Y1 T6	246	263	227	301	330	283	0,10	0,14	0,13
C24-X1 T6	279	284	273	342	352	335	0,09	0,11	0,10
C28-C2 T6	309	322	312	377	385	369	0,09	0,11	0,10
C20-Y1 T7	237	265	218	276	300	260	0,08	0,08	0,09
C24-X1 T7	270	257	263	335	352	334	0,09	0,13	0,10
C28-C2 T7	279	286	275	343	351	336	0,08	0,09	0,09

In the Table 4-5 the important tensile parameters of the flow curves are presented. As defined in the theoretical background section 2.9, these are True yield stress (YS), True stress at max load (TS) and True strain at max load (Eu).

The engineering stress-strain curves of all the T4 parallels are given in Appendix B.

4.5.1 Alloys vs alloys

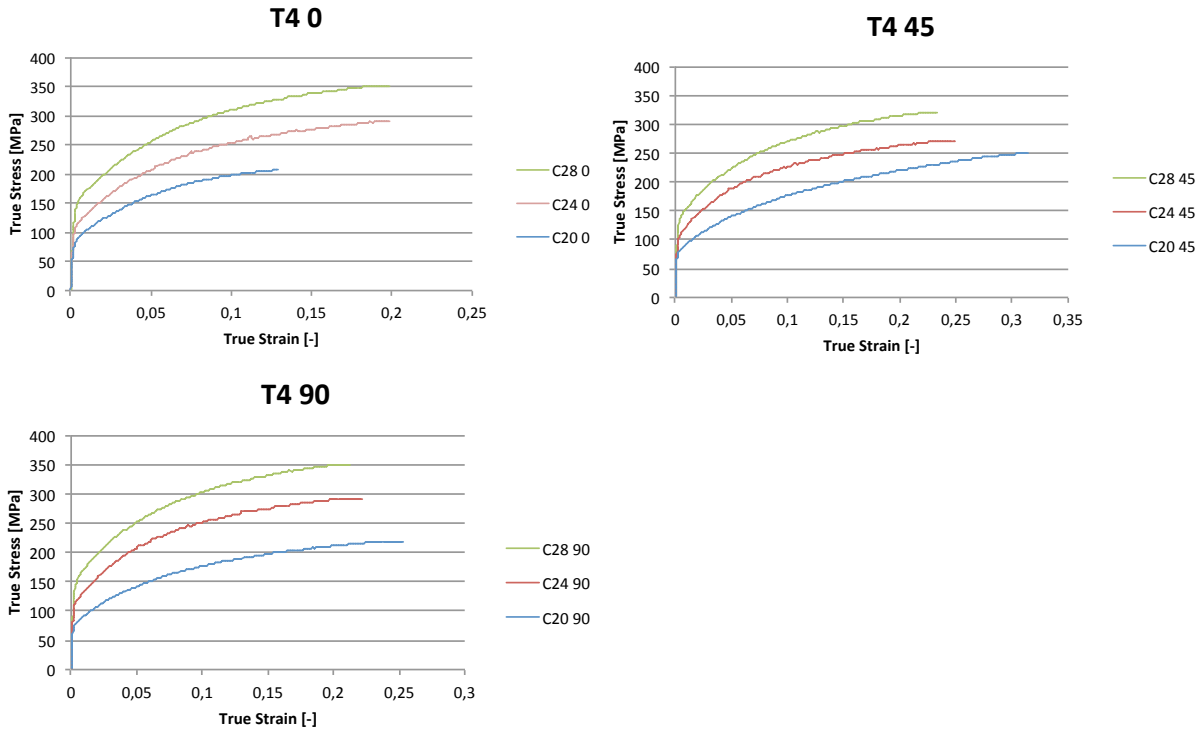

Figure 4-15: True stress-strain curves of all alloys and orientations at T4-temper.

The T4 flow curves in Figure 4-15 materials have a parabolic shape, indicating significant work hardening after the yield stress is reached. The C28-C2 alloy displays consistently the highest true yield stress (YS) and true stress at max load (TS). C24-X1 reaches a TS between 250-300 MPa dependening of the orientation. C20-Y1 shows the lowest strength of all the alloys. The latter is also seen to have the largest true strain at max load (Eu) in the 45- and 90-orientation. Due to experimental issues, the C20-Y1 0° curve should be viewed as unreliable. During the tensile test the fracture occurred outside of the extensometer, and not all the work hardening would have been recorded. The Eu reached by C24-X1 is seen to be systematically higher than Eu of C28-C2.

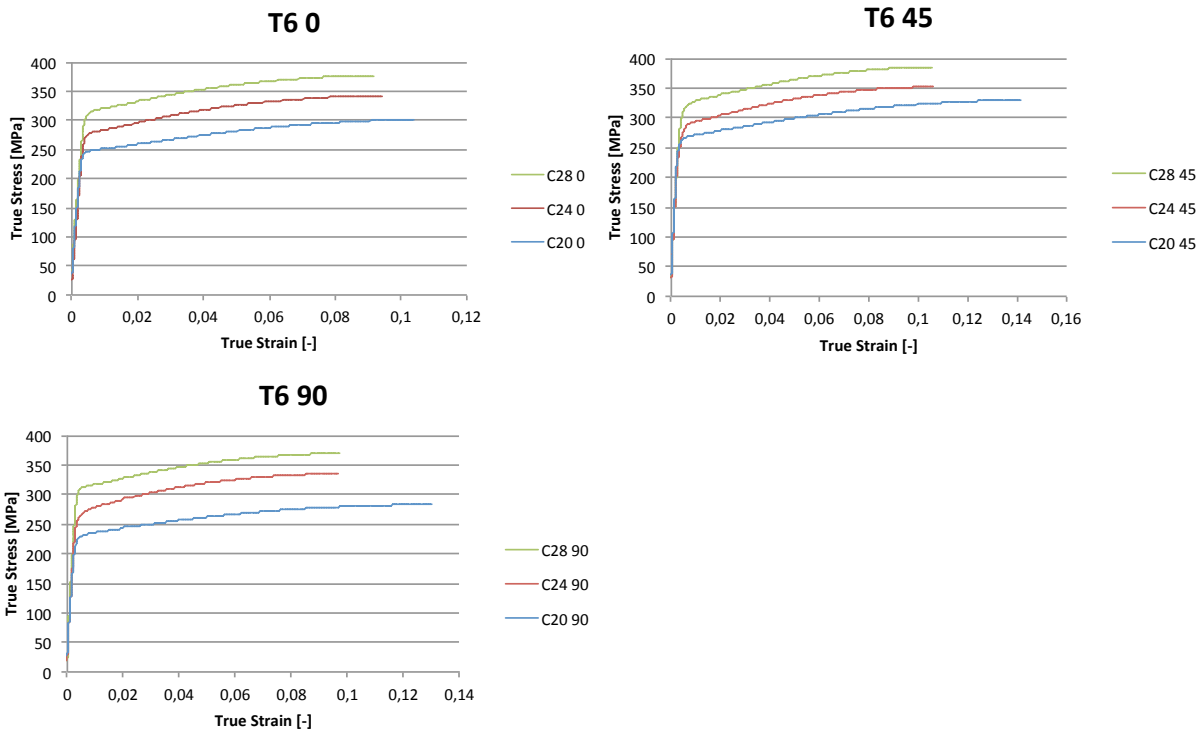

Figure 4-16: True stress-strain curves of all alloys and orientations at T6.

All flow curves of the T6-tempered materials show the C28-C2 alloy to be the strongest, including both true yield stress (YS) and true stress at max load (TS) (Figure 4-16). The C24-X1 comes in second and C20-Y1 in third in terms of strength. The difference in YS and TS, when comparing the alloys to each other, is significant. For example, the YS reached for the C20-Y1 0° is 246 MPa, 279 MPa for C24-X1 0° and 309 MPa for C28-C2 0°. This trend also applies for the different orientations. Furthermore, the amount of work hardening is seen to be similar for all the alloys. For the 0-orientated tensile specimens the reached true strain at max load (Eu) is ε = 0,10 for the C20-Y1 alloy and ε = 0,09 for both C24-X1 and C28-C2. The C24-X1 and C28-C2 show similar Eu in all orientations, which is seen to being smaller than the corresponding values of the C20-Y1 material.

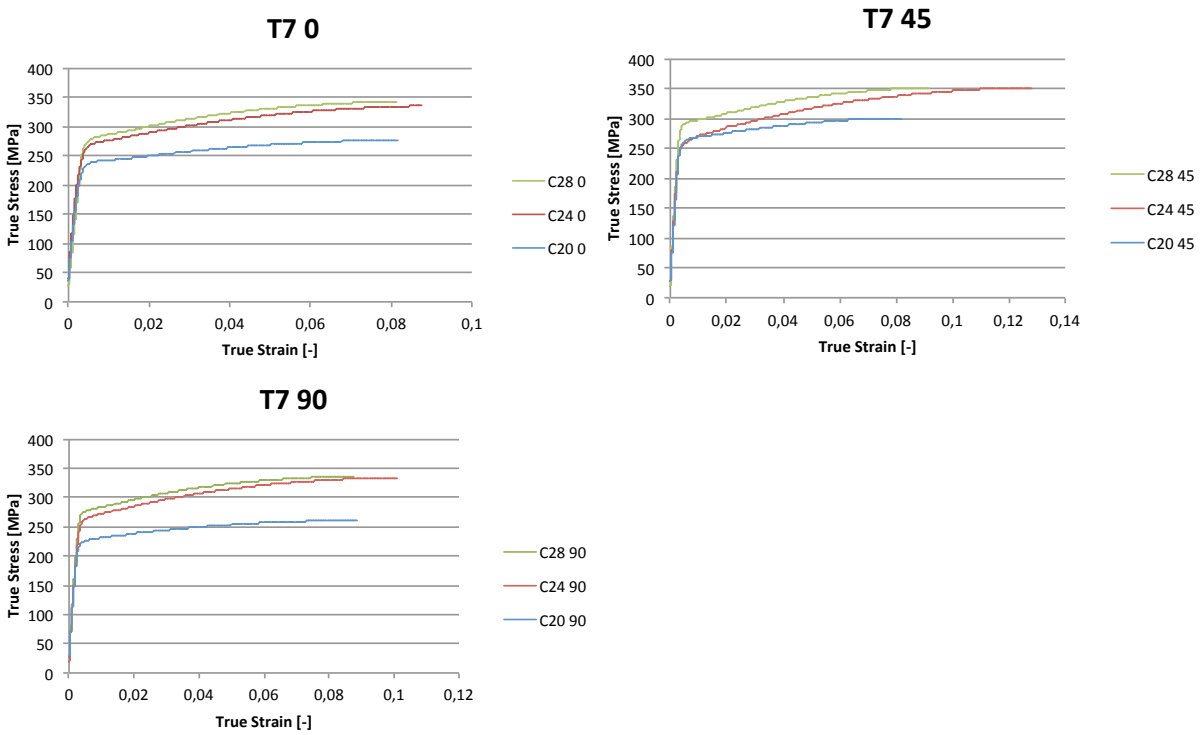

Figure 4-17: True stress-strain curves of all alloys and orientations at T7.

Finally the flow curves of the materials in the T7 temper state are considered in Figure 4-17. The systematic trend observed in the previous condition is again apparent. C28-C2 T7 show highest strength, followed by C24-X1 and when C20-Y1 T7 displays the lowest strength.

The YS of the C24-X1 and C28-C2 is almost equal, respectively 270 MPa and 279 MPa in 0°, and 263 MPa and 275 MPa in 90°. In these orientations the flow curves follow each other to the tensile point. The true yield stress (YS) of the C20-Y1 alloy is noticeably lower than the other alloys. In the 45° orientation however, the YS of C20-Y1 is close to the YS of C24-X1, and the true stress at max load (TS) of C24-X1 is close to the TS of C28-C2.

The true strain at max load (Eu) is seen to be largest for C24-X1 in all orientations. For the 0-oriented material, the Eu reached by C24-X1 is $\varepsilon = 0{,}09$, and the Eu of both C20-Y1 and C28-C2 is $\varepsilon = 0{,}08$. For these two last alloys, the Eu achieved is close to similar in all orientations.

4.5.2 Temper vs temper

In the following figures, the true stress-strain curves in different temper state are plotted against each other for each given alloy. The tempers of the C20-Y1 alloy are considered first, then C24-X1 and finally C28-C2.

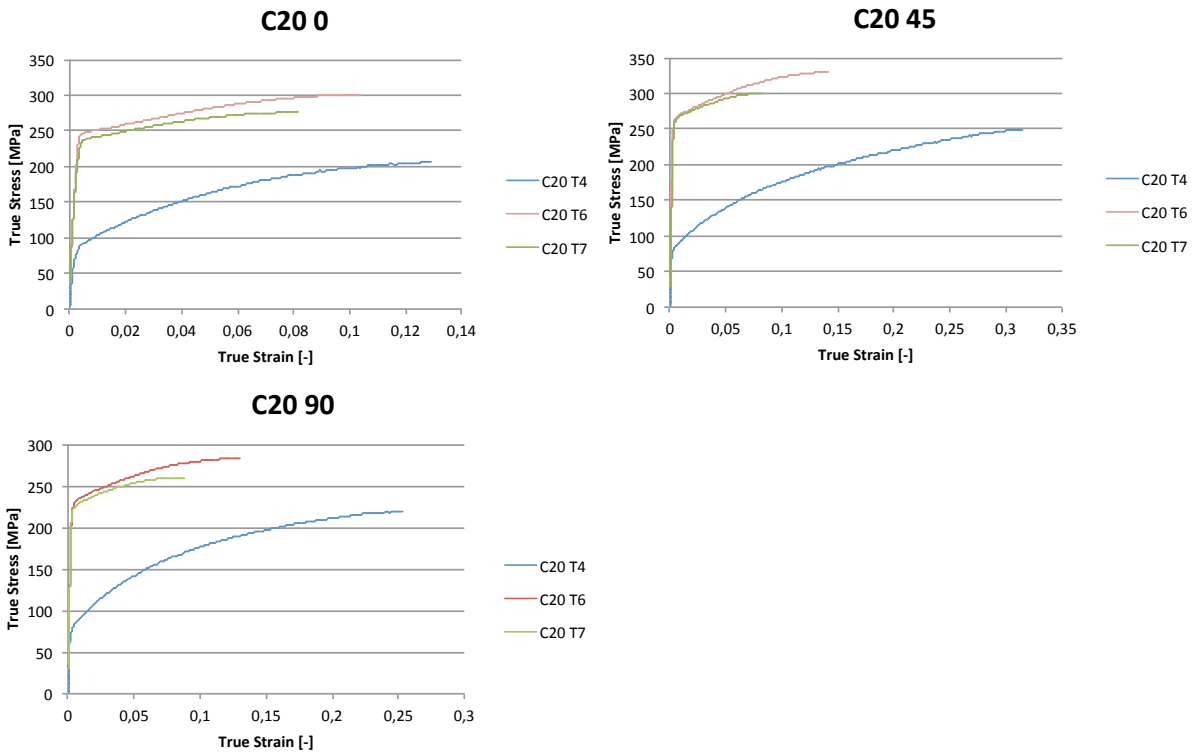

Figure 4-18: T4, T6 and T7 flow curves of the C20-Y1 alloy.

The flow curves in Figure 4-18 shows the T6-tempered C20-Y1 to be the strongest, although the true yield stress (YS) of C20-Y1 T6 and C20-Y1 T7 are close to similar. Between these two, more work hardening occurs for the alloys in the T6-temper. Both the true strain at max load (Eu) and true stress at max load (TS) of the T6-state exceeds the values of the materials in T7. The T4-tempered state has a clearly lower yield point, but much larger Eu than the other temper states. For example in 90-orientation, the C20 T4 yields at 95 MPa and reaches a TS of 219 MPa at Eu of $\varepsilon = 0{,}25$.

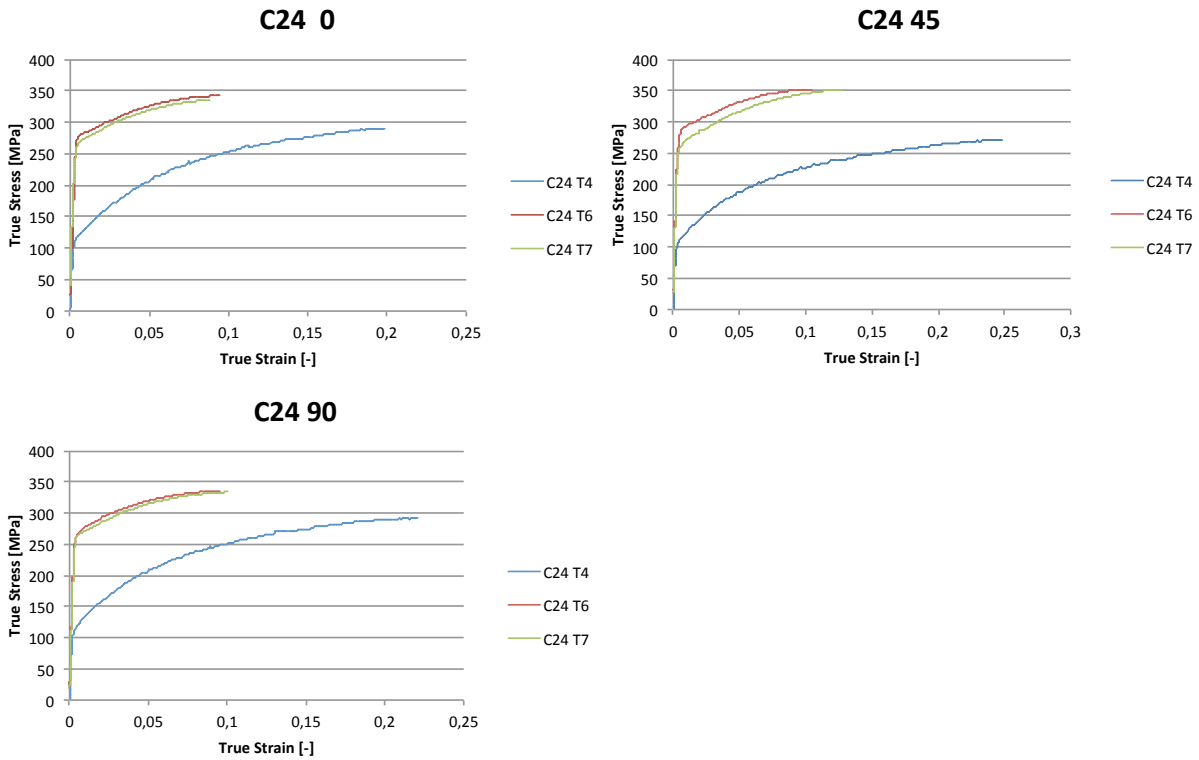

Figure 4-19: T4, T6 and T7 flow curves of the C24-X1 alloy.

In Figure 4-19 the tensile behaviour of C24-X1 in the different temper states is plotted. The conduct of the material is similar in the T6- and T7-state. These flow curves have almost identical shape, indicating that the true yield stress (YS), true stress at max load (TS) and true strain at max load (Eu) are almost similar. As seen for the C20-Y1 T4 Alloy, the C24-X1 T4 state is seen to have a large TS and Eu. The work hardening occurring for the materials in this temper state is obviously the most significant.

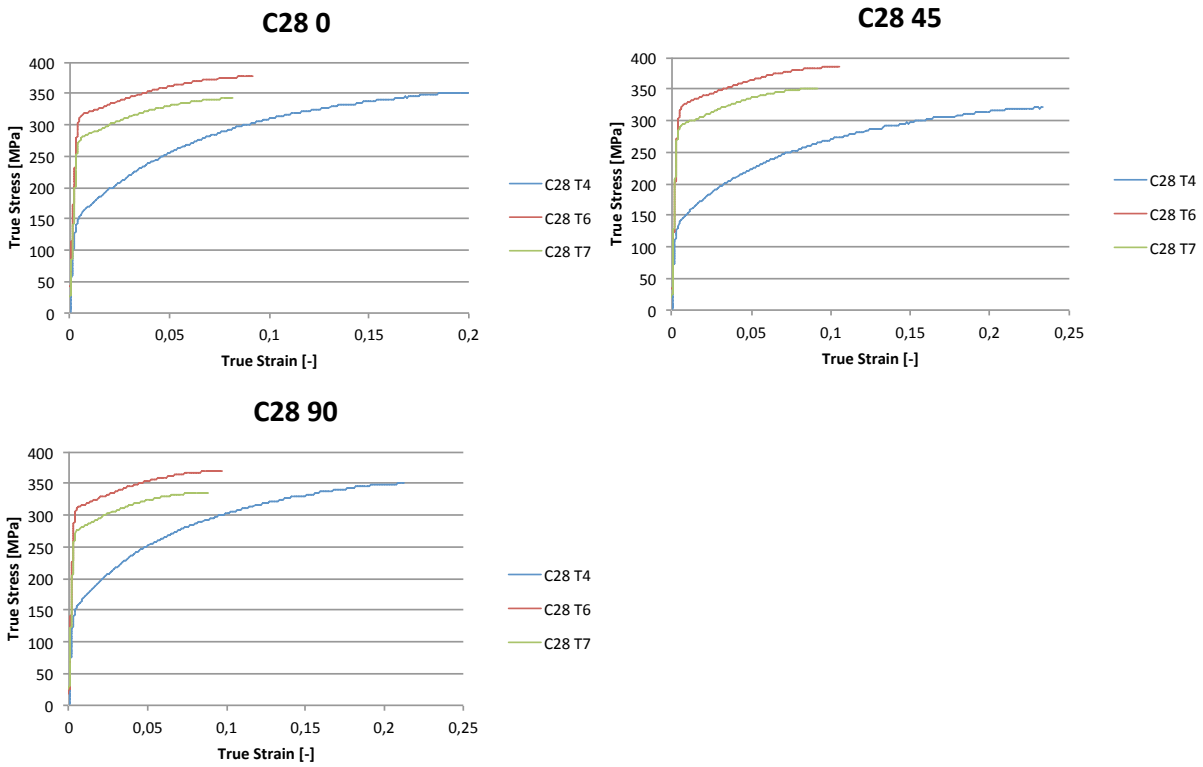

Figure 4-20: T4, T6 and T7 flow curves of the C28-C2 alloy.

The stress-strain curves of the tempered C28-C2 materials are plotted in Figure 4-20. The T6 state has systematically higher true yield stress (YS) and true stress at max load (TS) than is seen for C28-C2 T7. As seen for the other alloys, the alloy in the T4 state has the lowest YS but a high TS i.e the material undergoes much work hardening. In the 0- and 90-directions, the reached TS of C28-C2 T4 exceeds the TS of the material in T7-temper. The amount of work hardening in T6 and T7 tempers is seen to be relatively similar. Like the flow curves of C20-Y1 (Figure 4-18) and C24-X1 (Figure 4-19), the highest true strain at max load (Eu) occurs in the T4-state.

4.5.3 Anisotropy

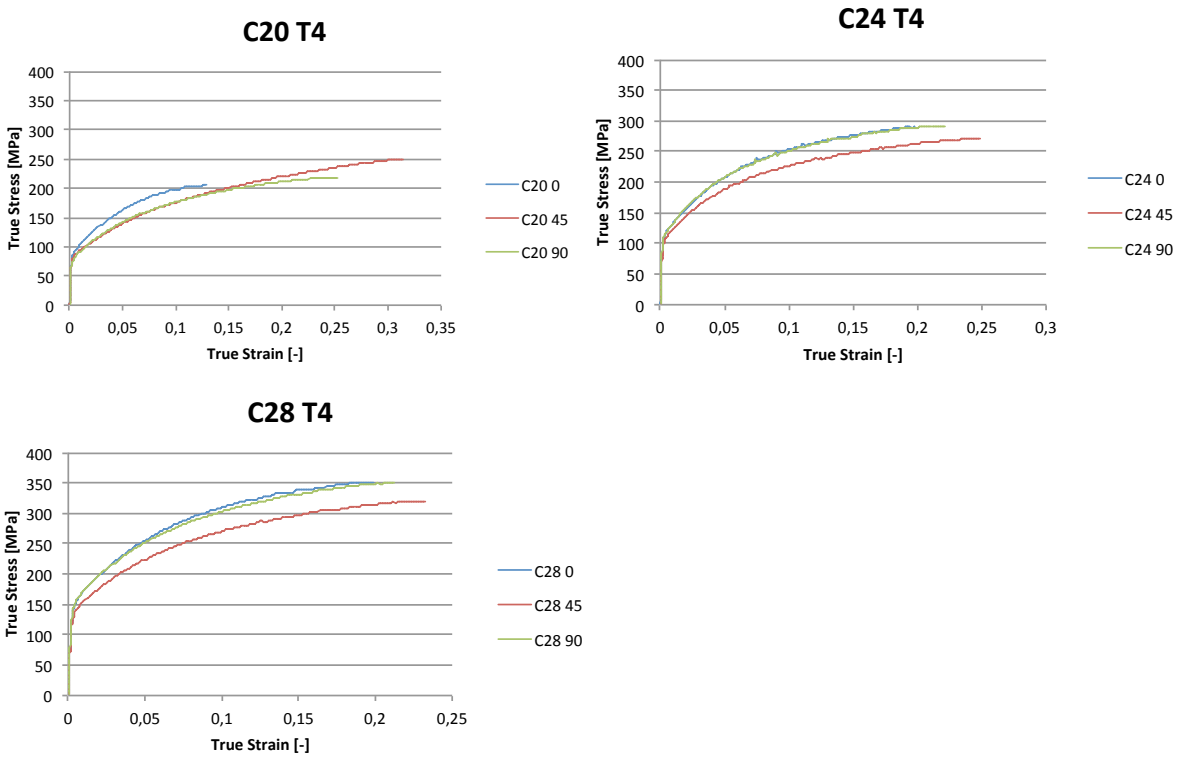

Figure 4-21: The T4-tempered materials, with the orientations plotted against one another.

The conduct of the flow curves in different orientations at T4 state is shown in Figure 4-21. The behaviour of C20-Y1 T4 0° is questionable as mentioned before, and will therefore be ignored here. For the recrystallized C20-Y1 the highest true yield stress (YS) and true strain at max load (Eu) is reached in the 45-orientation.

Similar tensile behaviour in the 0- and 90-orientation is noticed for C24-X1 T4. In these orientations the flow curves follow each other to the tensile point. This trend is noticed also noticed for C28-C2 T4. The 45-oriented material shows lower true stress at max load (TS) than the other orientations, but reaches higher a Eu. This is again seen for both fibrous alloys.

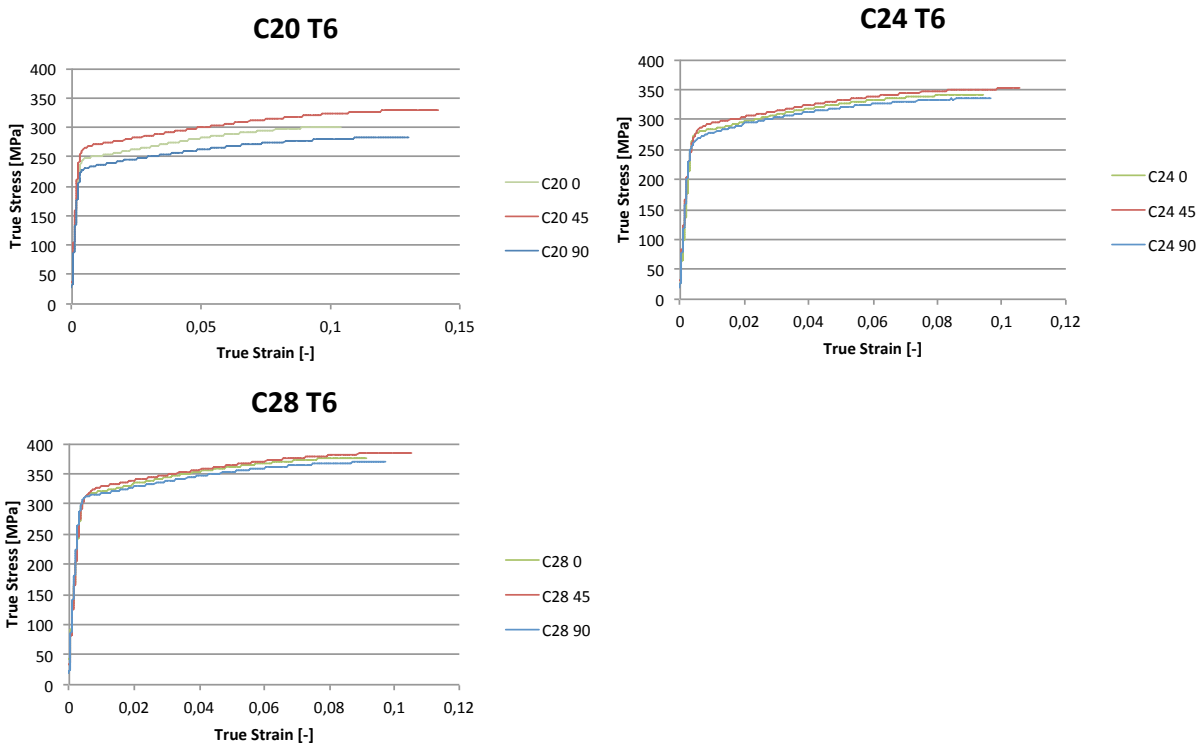

Figure 4-22: The T6-tempered materials, with the orientations plotted against one another.

In Figure 4-22 the true stress-strain curves in the different orientations at the T6-temper state. Several general remarks can be made about the anisotropy of the alloys at T6-state. A systematic trend is seen as the 45-orientated materials display highest true yield stress (YS) and true stress at max load (TS). The second highest strength is reached in the 0-orientation, and finally the 90-oriented materials display the lowest strength. Another systematic trend is with respect to the true strain at max load (Eu) of all the alloys, as the order from largest to lowest Eu is seen to be 45, 90 and 0.

For the C20-Y1 alloy there is a pronounced difference in YS and TS between the different orientations. In 0-orientation the YS obtained is 246 MPa, 263 MPa is acheived in the 45-orientation and 227 MPa in the 90-orientation.

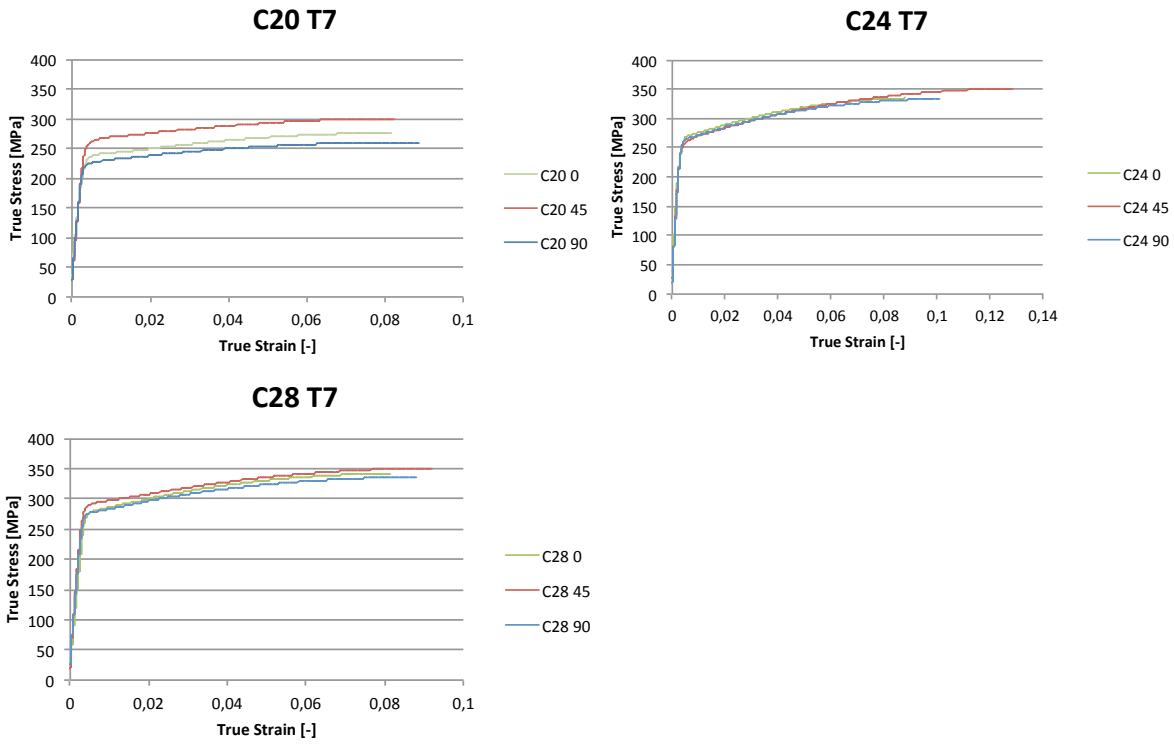

Figure 4-23: The T7-tempered materials, with the orientations plotted against one another.

Finally the anisotropy of the alloys is considered in the T7-temper state in Figure 4-23. The 45-oriented materials again display the highest strength, followed in order by the 0- and the 90-orientation.

Like in the T6-state, a significant difference in true yield stress (YS) and true stress at max load (TS) is noticed for C20-Y1 T7. In other words the anisotropy of this alloy is significant. Again, C24-X1 and C28-C2 behave quite the same, i.e. the tensile properties for the fibrous alloys are similar in the different orientations.

4.6 Flat profiles vs Box profiles (taken from M4)

An important objective of this thesis is to compare the properties of the flat profiles to the 2-chamber box profiles for the same material and temper conditions. The true stress-strain curves of the box profiles are taken from the project by S.Dumoulin et al. entitled: "*Dynamic and quasi-static crash preformance of aluminium extrusions: summary of students screening tests"*[2]. The notation used for the different tempers in this project is different than in this thesis. For C20-Y1, the box-profiles are referred to as V7-S0 for the T6 temper state, and V7-S1-1 for the T7-state [2]. However, to facilitate the comparison the same colour is used for the materials subjected for same heat-treatment.

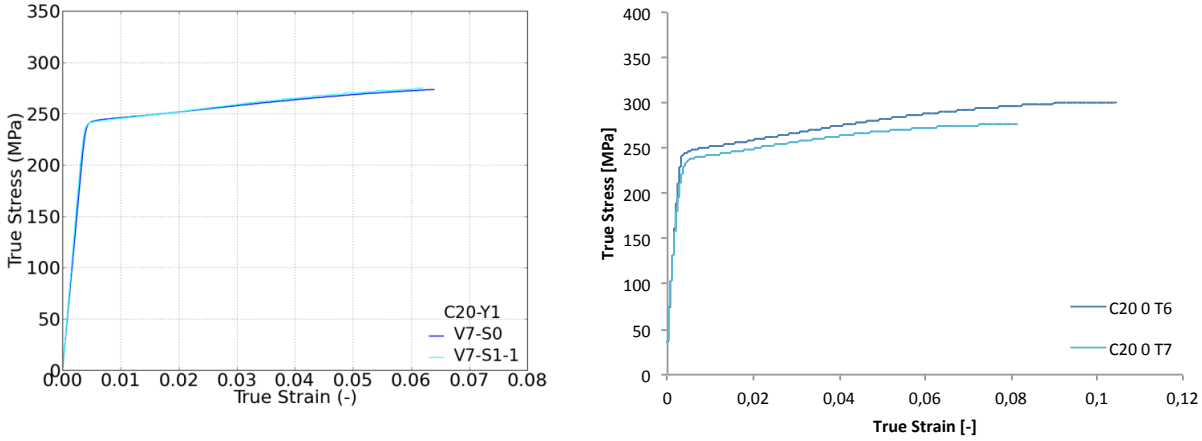

Figure 4-24: True stress-strain curves of box profiles V7 (C20-Y1) to the left (taken for Figure 7 in [2]), and to the right the curves of the flat profiles.

The stress strain curves of the box profiles and the flat profiles are presented in Figure 4-24. The heat-treatment of V7-S0 is the same as for C20 T6, and the V7-S1-1 the same as C20 T7.

When comparing the two graphs the major difference is seen in the reached true strain at max load (Eu). The flat profiles achieve much higher Eu, to a value of almost the double in size. No substantial difference in strength is noticed between the two types of profiles. The difference between T6 and T7 is significant for the flat profiles, a difference not seen in the box profiles.

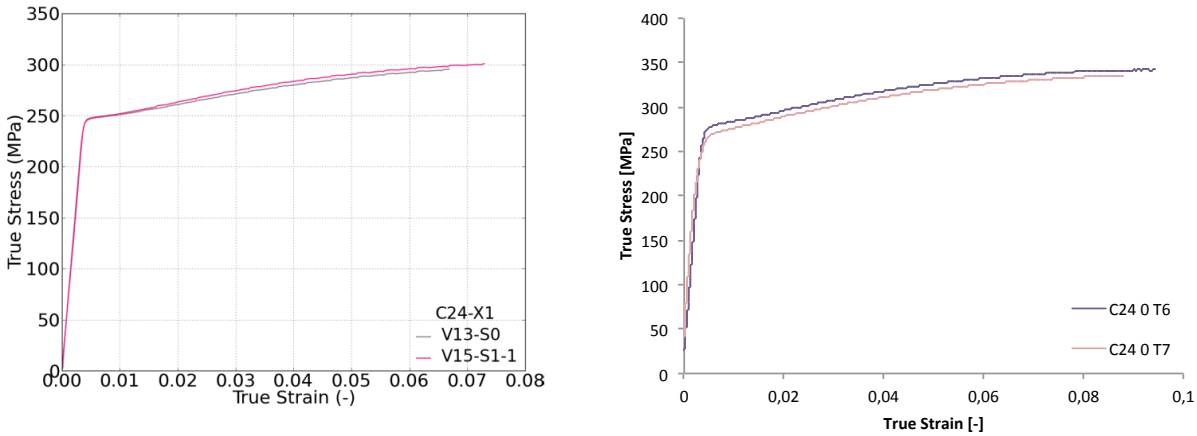

Figure 4-25: True stress-strain curves of box profiles V13 (C24-X1) to the left (taken for Figure 7 in [2]), and to the right the curves of the flat profiles.

The juxtaposition of stress-strain curves of the C24-X1 alloy is shown in Figure 4-25. Again the achieved true strain at max load (Eu) is somewhat larger for the flat profiles. Here, the reached true yield stress (YS) and true stress at max load (TS) are clearly higher for the flat profiles for each respective temper state. The flat profiles at the T6- and T7-state are seen to behave similarly in terms of stress-strain behaviour, although the latter state shows slightly less strength.

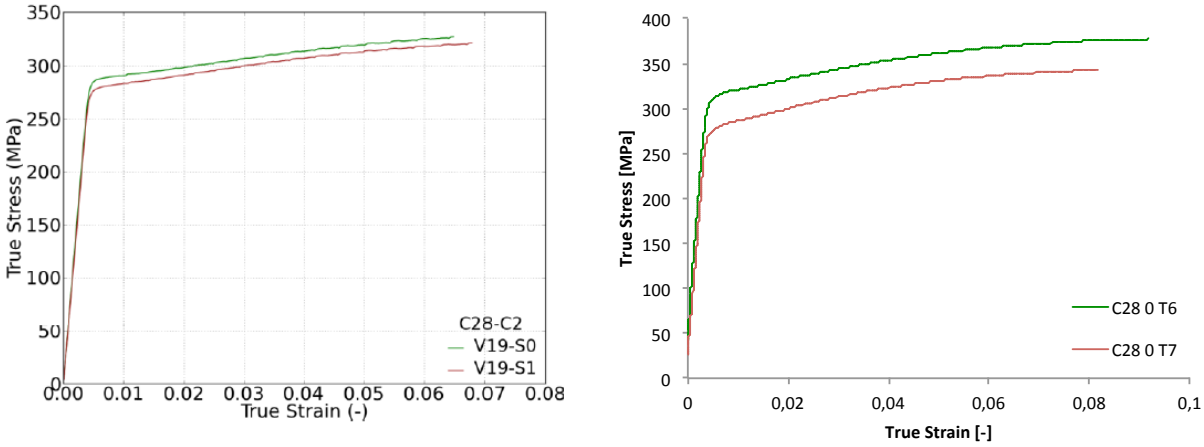

Figure 4-26: True stress-strain curves of box profiles V19 (C28-C2) to the left (taken for Figure 7 in [2]), and to the right the curves of the flat profiles.

For the C28 and V19 alloy the same trend noticed for the other alloys are observed, as the Eu reached in flat profiles are higher than for the box profiles. In terms of strength the materials in the T7-state (V19-S1 and C28 T7) perform similarly. However the C28 T6 alloy displays higher strength than its box profile counter part.

4.7 Bending test

The calculated average bending angles at maximum force are presented the in following figures. As three parallels for each specific alloy, temper and orientation were used, one angle is plotted for each parallel. Equation (2-10) was used to calculate the angles. The figures include an error bar, representing the standard deviation of the calculated angles. The force-extension curves of all the parallels are given in Appendix C.

4.7.1 Alloy vs Alloy

First, the bendability of each alloy is considered. The bending angles α are plotted for each alloy at a specific temper. First the angle α reached by the materials in the T4-temper state are presented, then at T6 and finally at T7.

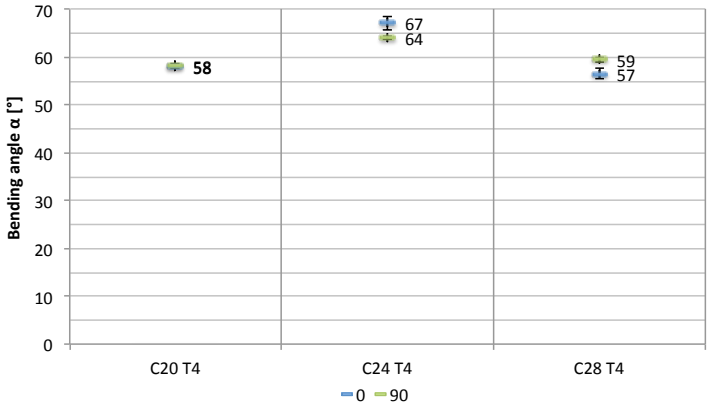

Figure 4-27: The bending angles reached in the T4-temper state.

In the T4-state the C24-X1 alloy, as seen in Figure 4-27, reaches the highest bendability. C20-Y1 to reaches the same angle α in both orientations. C28-C2 achieves 59° in 90-orientation and 57° in 0-orientation. The highest angle α is reached in the 0-orientation, for the C24-X1 alloy.

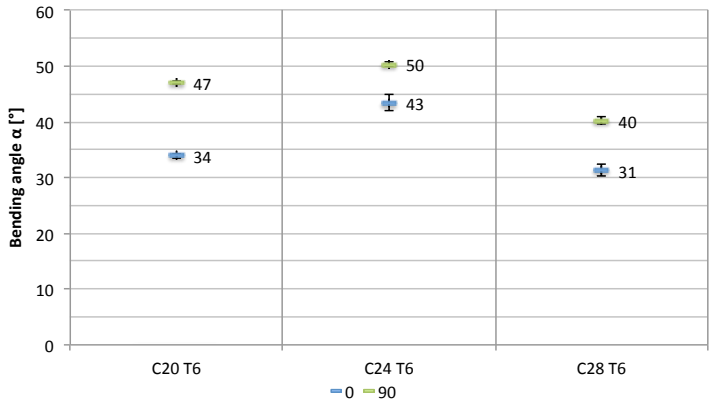

Figure 4-28: The bending angles reached in the T6-temper state.

The highest angles α are seen in the 90-orientations for materials in Figure 4-28. Here, the C28-C2 alloy performs the worst. Again the C24-X1 reaches highest α in both orientations. The anisotropy, i.e. the difference in α reached in the two different orientations is smallest for C24-X1. The highest anisotropy is seen for C20-Y1.

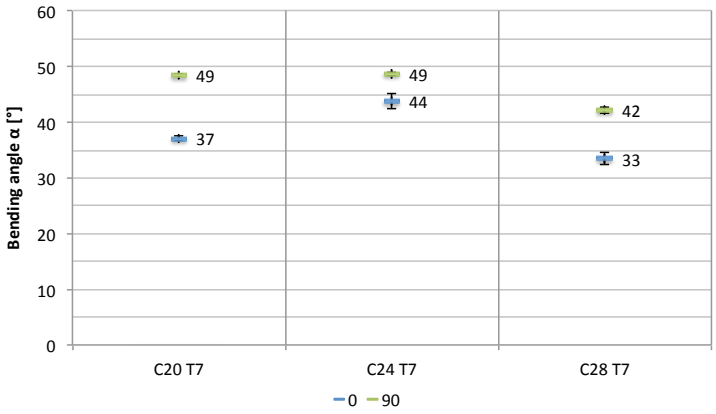

Figure 4-29: The bending angles reached in the T7-state.

In Figure 4-29 the results of the bending test of T7 temper state are displayed. As previously seen in the other tempers, C24-X1 reaches again highest α in both orientations. C28-C2 achieves lowest bendability and the highest anisotropy is seen for C20-Y1.

4.7.2 Temper vs temper

In this section the bending angle α is evaluated and compared for the different tempers. First the C20-Y1 alloy is considered, followed by C24-X1 and C28-C2.

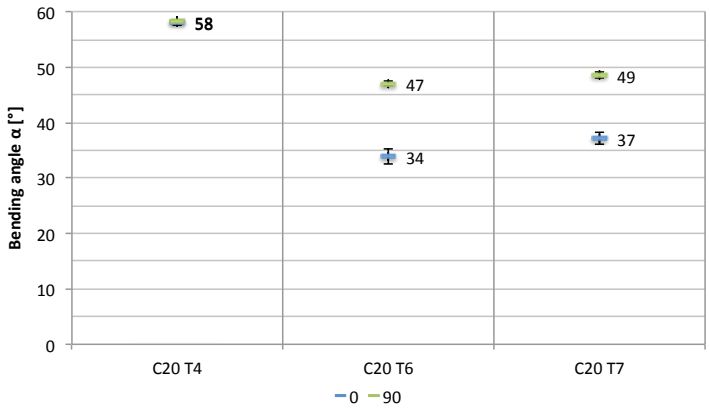

Figure 4-30: Bending angles of C20-Y1 in the different tempers.

Both the lowest anisotropy and highest bending angles are reached in the T4-state seen in Figure 4-30. The highest anisotropy is seen at T6 temper, as the difference in α (90- – 0-orientation) is seen to be 13°. In the T7-state the difference between α is seen to be 12°.

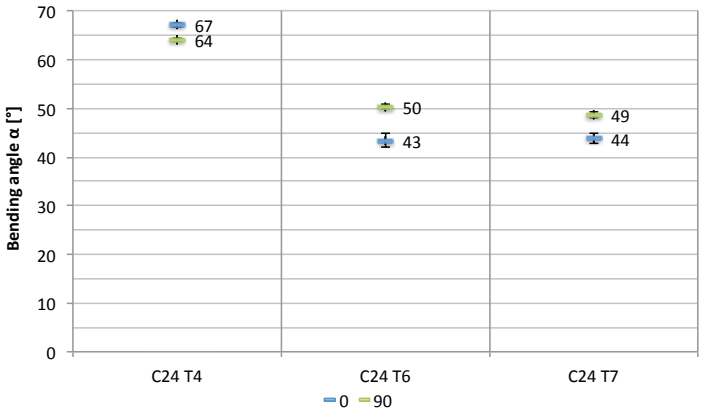

Figure 4-31: Bending angles of C24-X1 in the different tempers.

Figure 4-31 representing alloy C24-X1 shows the same trend as for C20-Y1, as T4 has the highest bendability and lowest anisotropy. The angles reached in T6 and T7 are seen to be close to the same. Only one degree separates the angle α in the respective orientation.

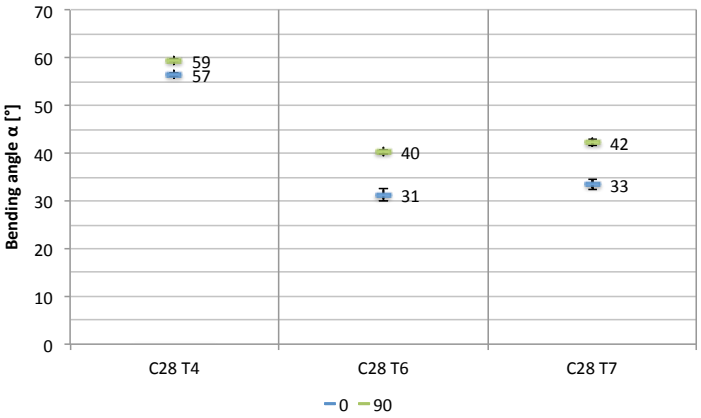

Figure 4-32: Bending angles of C28-C2 in the different tempers.

For the C28-C2 materials in Figure 4-32, again the same trend is observed as the lowest anisotropy occurs for the T4-tempered materials. The differences between the T6- and T7-tempers are small. In the T7-temper state the C28-C2 alloy performs slightly better in both orientations.

4.7.3 Flat profile vs box profiles

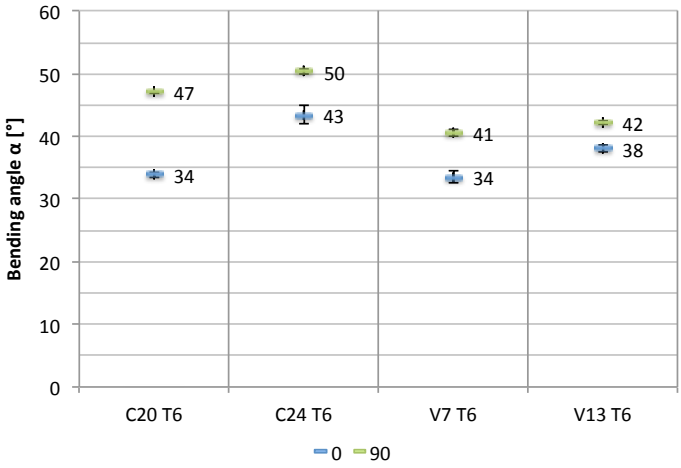

Figure 4-33: Bending angles of the box profiles and flat profiles in T6-temper state.

The bending angles α of the box profiles and the flat profiles are presented in Figure 4-33. The highest bending angles are seen for C24-X1 T6 flat profile and V13 (C24-X1) box profile, although highest angles are reached for each by the flat profile. A similar trend is noticed for C20 T6 and V7 T6. In the 0-orientation the angles reached are the same for each profile 34°, but in the 90-orientation the flat profile outperforms the box profile.

Generally speaking the highest amount of anisotropy, i.e. differences in bending angle is seen for the flat profiles. When considering the anisotropy of the profiles, it is seen that the C20-Y1 alloy (both C20 T6 and V7 T6) displays the largest difference in bendability.

5 Discussion

The characterization of the microstructure, texture and particles of the aluminium alloys are discussed first. These results are then used as basis to discuss the mechanical behaviour of the extruded profiles. Based on the stress-strain curves and bending test presented, the objective is to highlight differences between the alloys, the tempers and the properties in the different orientations.

5.1 Characterization of the material

The microstructure of the materials are considered first, followed by the crystallographic texture of the recrystallized C20-Y1 and the fibrous alloys. Finally the characterization of the primary particles is evaluated.

5.1.1 Microstructure.

The characterization of the microstructure shows a recrystallized C20-Y1 alloy and fibrous C24-X1 and C28-C2 alloys. When comparing the two fibrous alloys the recrystallized surface layer is larger for the C24-X1 alloy. As these two alloys contain a larger amount of alloying elements forming dispersoids such a microstructure is expected. Elements like Mn and Cr are known to form finely dispersed dispersoids that may slow down and even inhibit recovery, recrystallization and grain growth in aluminium alloys, as mentioned in the theoretical background section 2.5.

The C24-X1 alloy showed no sign of change in microstructure after heat-treatment at 540° C. It is therefore assumed that no real difference in microstructure and texture exists between each temper, and most important a W/T4 condition can be re-solutionized from aged tempers without affecting the fibrous microstructure.

5.1.2 Texture of recrystallized C20-Y1

The pole figure developed from the EBSD scans of the C20-Y1 T6 alloy show a dominant {001}<100>-cube texture in middle of the ED-ND cross-section, and a {001}<110>-rotated cube texture in top surface layer. The cube texture is an often obtained as the recrystallized texture upon annealing after plain strain deformation of aluminium alloys [8].

The difference in crystallographic texture on the top surface layer and middle layer is due to different deformation mechanisms prior to recrystallization. Shear strain is common near the surface of extruded parts. The study of texture development in shear strain is complex and

limited literature on the matter exists. The evolution of a dominated rotated cube texture in rolled aluminium has been seen to appear in the surface layer previously [13].

5.1.3 Texture of fibrous alloys

The fibrous C24-X1 and C28-C2 alloys are seen to have similar pole figures in the middle of the cross-section. The deformation texture include different types of crystallographic orientations, in this case: a strong {110}<112> Brass is seen. These textures are typically seen in cold worked aluminium parts. [8] Also some {001}<100> Cube texture is seen in the ODF. The cube texture is not a typical deformation texture, it might be speculated that some recrystallization has taken place during extrusion.

In the surface layers of these alloys the pole figures indicate a strong {011}<112> Goss-texture in addition to some rotated cube texture. Generally the differences between the ODFs of each fibrous alloy are small.

5.1.4 Particle Characterization

The primary particles of the different alloys are seen to be different. The largest primary particles are found in the C28-C2 alloy, and the smallest particles are seen in C20-Y1. Differences in size are linked to the chemical composition of materials, as the material with highest amount of alloying elements (C28-C2) contains the largest particles. On the other end of the spectrum the low-alloyed C20-Y1 shows lowest average particle size. The particles seem to be systematically elongated in the ED. This trend is presumed to occur during extrusion on pre-existing segregations precipitated during casting.

5.2 Tensile properties

The mechanical properties observed form the true stress-strain curves are considered in this section. The structure of the discussion follows the corresponding section in the results chapter.

5.2.1 Comparison of the alloys

In this section the tensile properties of the alloys are compared to each other at a specific temper and orientation.

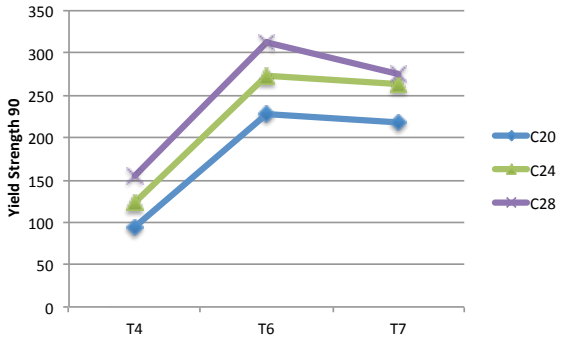

Figure 5-1: True yield stress (YS) of the alloys in 90-orientation.

Figure 5-1 shows the true yield stress (YS) of the 90-orientated tensile specimens. The 90-orientations is chosen to illustrate the difference between each alloy, as they perform qualitatively similarly in the other orientations as well. The high-alloyed C28-C2 alloy outperforms the two other alloys in all temper states respectively. The YS of C24-X1 is the second highest, followed by the C20-Y1 alloy.

As the amount of restrictions, created by the alloying elements, on the dislocation movement increases a larger force requirement is needed to move the dislocation. In the T4 temper this is mainly due to differences in solid solution hardening. In the T6 and T7 a significantly higher strength is obtained due to precipitation hardening.

A fall of strength is seen for the C28-C2 alloy at T7-temper state, as it displays similar YS as C24-X1 T7. This reduction of strength is further discussed when comparing temper states.

Another noticed trend is the similar work hardening occurring in each alloy. For example the difference in YS between C20-Y1 and C24-X1, is almost equal to the difference in true stress at max load (TS) between C20-Y1 and C24-X1. This leads to the assumption that the work

hardening occurring in the materials is less dependent on the starting chemical composition, and more on the thermo-mechanical processing of the profiles.

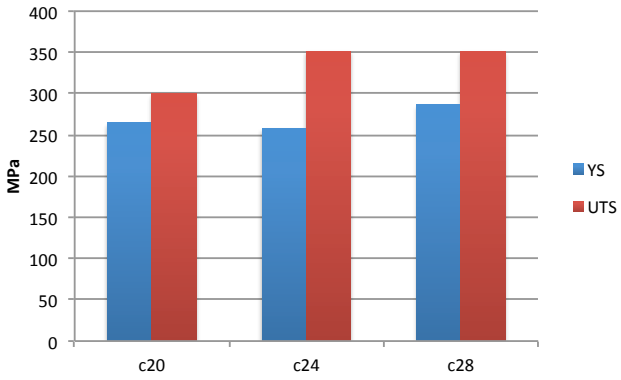

Figure 5-2: The true yield strength (YS) and true stress at max load (TS) for the 45-orientated T7 alloys.

One exception is seen for the 45-orientated T7 tempered materials. Figure 5-2 illustrates larger work hardening occurring for the C24-X1 alloy, compared to the two others. It should be pointed out, that this exception only occurs for the 45-orientated T7-tempered materials. The reason for this exception is difficult to pinpoint. The mechanical properties of the alloys might experience a deviation in this specific orientation and temper, or this might be due to an experimental error.

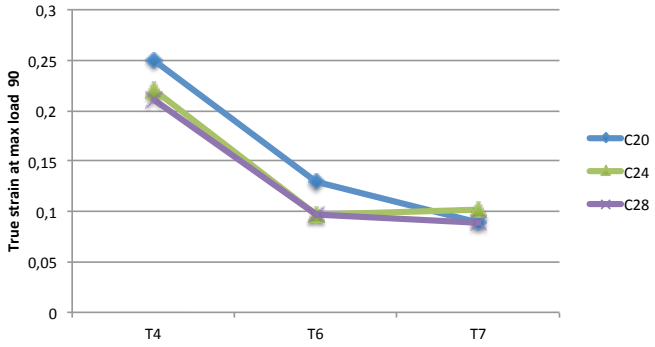

Figure 5-3: True strain at max load (Eu) for 90 orientated materials.

In the Figure 5-3, the true strain at max load (Eu) of different alloys in the 90-orientation is plotted. A trend of C20-Y1 reaches the highest Eu is seen in the T4- and T6-temper states. The curves of C24-X1 and C28-C2 follow each other in these tempers. For the T7-tempered alloys the strain is seen to cluster around the same value, although C24-X1 displays a slightly higher Eu.

The results indicate the recrystallized C20-Y1 material behaves slightly better than the two fibrous alloys. The subgrain structure of the fibrous alloys are expected to give a loss in

ductility. The observed lower Eu is an indication of this. It should be pointed out that true strain at maximum load (Eu) is not a perfect parameter of ductility. Better descriptions of ductility like elongation at fracture and reduction of area, were unfortunately not evaluated in this study.

Dorward et al. concluded in their study that lean (0.78 wt% Mg and 0.53wt% Si) and nominal (0.93 wt% Mg and 0.63 wt% Si) balanced chemistries give a aged combination of strength and toughness. [17] The composition of the C24-X1 alloy (0.71 wt% Mg and 0.57 Si) resembles the composition of the mentioned alloys, and seems to have the best combination of YS, TS and Eu. Although this comparison is superficial, there seems to be a correlation between this thesis and the results of Dorward et al.

5.2.2 Effect of Temper state

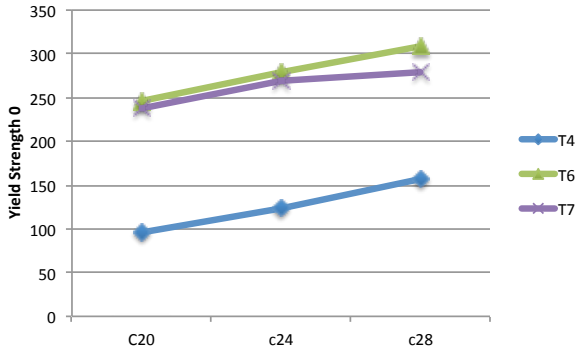

Figure 5-4: Yield Strength at the different tempers in 0-orientations.

The general trend shows the T6-tempered materials to have the highest true yield stress (YS) and true stress at max load (TS). The T7 materials are seen to have slightly lower YS. Finally the T4 alloys yields at the lowest stress. This systematic difference is highlighted in Figure 5-4. The peak aged T6 materials obviously contain the most beneficial precipitation structure. These alloys are expected to perform the best in terms of strength, as the most optimal precipitate structure is achieved. As mentioned in the experimental section 3.1, the T6 materials are aged at 185° C for 6 hours, and T7 materials aged at 205° C for 2 hours. The over aged T7-state would have a precipitation structure close to that of T6, with a somewhat lower strength, as peak strength is reached faster.

The materials in T4-temper were not subjected to artificial age hardening although some natural ageing is expected to have occurred consistent with the temper designation i.e natural ageing. As the material was heat treated and quenched within 24 hours of the tests some

natural ageing would be expected. The test specimens would contain some amount of GP-zones or early stage precipitates, however still with most of the alloying elements in solid solution.

The YS of the C28-C2 T6 and C28-C2 T7 are seen to be significantly different in Figure 5-4. This phenomenon is not seen for the two other alloys, as the yield point remains similar. The flow curves of T7-tempered C28-C2 alloy show a significant loss of strength when comparing it to the T6-temper. This is an indication that C28-C2 reaches peak strength earlier than the other alloys. This trend is clearly seen in the 0 and 90 orientations.

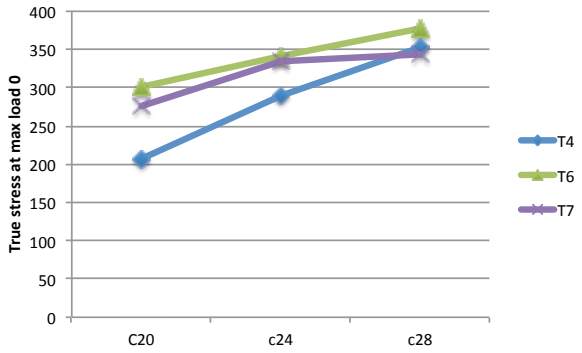

Figure 5-5: The true stress at max load (TS) in the 0-orientation.

Several observations are made when considering the TS at the different tempers. Figure 5-5 shows that the highest TS attained in the T6-tempered materials. The TS of C28-C2 experiences a dive in T7. For this alloy the tensile strength is even higher in T4 than in T7, again a clear indication of the fast over aging in C28 as mentioned above.

The amount of work hardening occurring in the T4-tempered materials is significantly larger than in the other states. When comparing the YS (Figure 5-4) and the TS (Figure 5-5), it is seen that the T4 condition has the most pronounced evolution from YS to the TS, consistent with the significant work hardening.

A general distinction can be made about the TS of C20-Y1, as it is heavily affected by its temper state. The difference in TS between C20-Y1 T6 and T4 is about 100 Mpa. For the C28-C2 alloy the difference between the highest and lowest TS observed is seen to be less than 30-40 MPa.

This indicates that the TS of low-alloyed materials like C20-Y1 is highly dependent of the heat-treatment. Whereas C28-C2 reaches approximately the same TS regardless of temper state. This is due to much faster natural aging in the higher alloyed materials, reducing the subsequent precipitation hardening effect during artificial ageing.

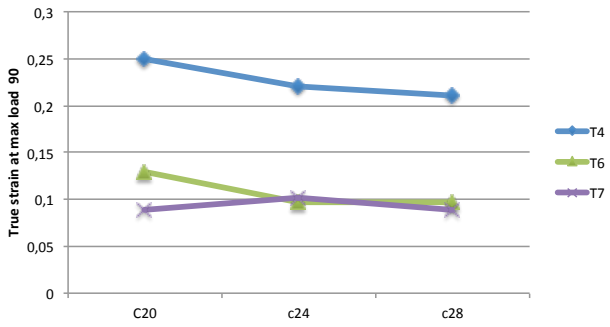

Figure 5-6: The true strain at max load (Eu) in the 90-orientation.

Materials in the T4-temper state are seen to always display the highest true strain at max load (Eu) and the most work hardening. Figure 5-6 demonstrates how much larger the strain reached is in T4 than in the other tempers. The shape of the curve of the T7-state true strains is seen to be dissimilar from the others. As seen the Eu reached by C20-Y1 T7 is significantly different from the Eu of C20-Y1 T6. Based on these results, the ductility of the fibrous alloys appear to be less affected by the precipitation structure than the recrystallized C20-Y1.

5.2.3 Anisotropy in tensile properties

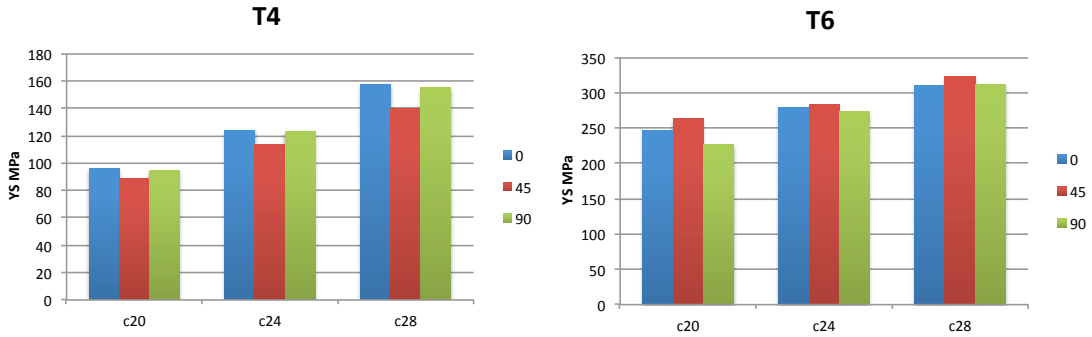

Figure 5-7: Yield Strength in the different orientations. To the left the T4 materials and to the right the T6-materials.

In Figure 5-7 the YS in the different orientations is displayed in T4 and T6. The behaviour of the tensile properties for the artificially aged materials is seen to be similar. With this in mind the T6-temper state will represent the artificially aged materials, and compared to the T4-temper state.

In the T6 temper state, the general trend shows the 45-orientation to reach the highest yield point, followed by 0 and finally 90. For the T4 tempered materials the 45 orientations shows the lowest YS. The precipitation structure in the different materials is assumed to be the cause of this variance in anisotropy, as the texture is assumed to be the same in the different tempers.

The anisotropy of the material C24-X1 and C28-C2 is seen to be low in T6. The C20-Y1 alloy on the other hand yields at significantly different values for each orientation.

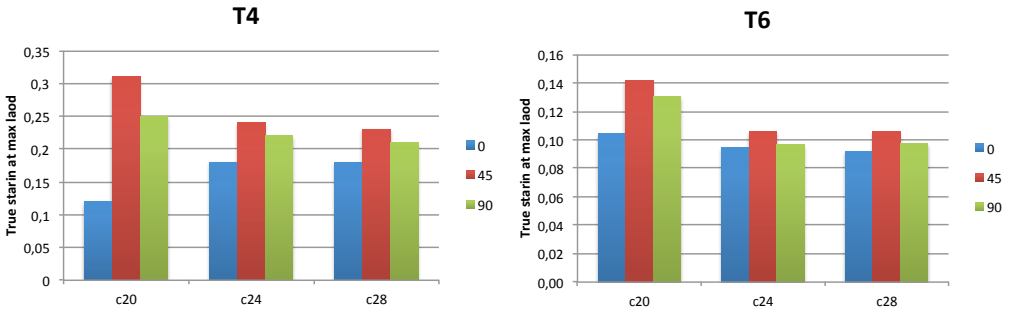

Figure 5-8: True strain at max load in the different orientations. To the left the T4 materials and to the right the T6-materials.

The general trend observed from the flow curves is maximum true strain is seen in the 45 orientation. The 0-orientation shows the lowest Eu for all orientations. It should be noted that the difference in values of Eu in the different orientations is not very pronounced.

Another trend is seen when comparing the recrystallized C20-Y1 T6 to the fibrous C24-X1 T6 and C28-C2 T6. A great amount of anisotropy is seen in the recrystallized alloy and not in the fibrous. The flow curves of the fibrous materials are close to equal at a given temper. The explanation to this phenomenon is linked to the interaction of the dislocations and their slip systems on the microstructure and texture of the C20-Y1 alloy. As both large recrystallized grains and a dominant Cube texture are likely to individually play role on the anisotropy of the material the issue becomes quickly very complex.

5.2.4 Comparison of the different profiles

When comparing the tensile properties of the flat profiles and the box profiles a systematic difference is noticed. The reached true strain at max load (Eu) is always seen to be higher for the flat profiles. As the geometry of the profiles is different, the deformation during extrusion is expected to affect the mechanical properties differently.

The V7 box profile and the C20 flat profile display similar strength. The true stress-strain curves of the box profile in T6 (V7-S0) and T7 (V7-S1) are seen to follow each other to TS. A slight difference in strength is noticed for the flat profiles as the C20-T7 yields at lower strength, and a reaches a lower TS than C20 T6.

The V13 box profile displays lower strength than it flat profile counter part C24. This is seen in both temper states, as V13-S0 performs worse than C24 T6 and V15-S1 worse than C24 T7. As for the high-alloyed C28-C2, the highest strength is seen in flat profiles in T6 tempers. As discussed earlier the C28 T7 flat profile experiences a loss in strength. In this temper state the box profile and flat profile display similar strength.

5.3 Bending test

The results of the three point bending test are evaluated in this section. First the general bendability is discussed for the different alloys and then the anisotropy of different alloys is considered.

5.3.1 Bendability

The bending test is used to determine the bendability of the material. The bending test is generally considered to be more representative test of formability than tensile testing above. In contrast to the tensile test, only the 0 and 90 orientations are tested.

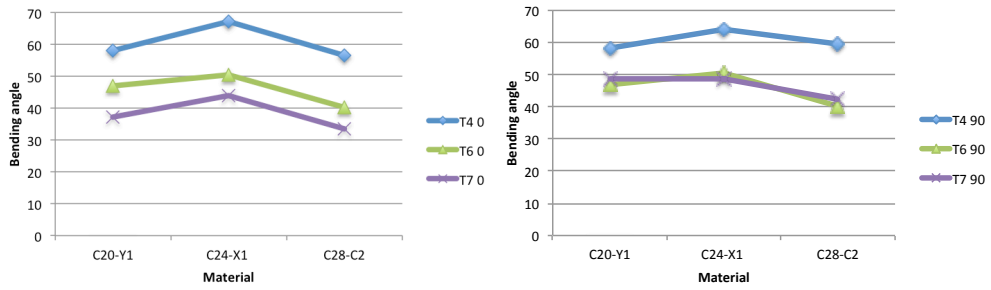

Figure 5-9: Reached bending angles of the different tempers. To the right: 0-orientation and to left: 90-orientation.

The T4-tempered alloys have best bendability as seen by the large bending angles, followed by T7-tempered material and finally the T6-tempered materials. Furthermore the good bendability of the T4 materials might be caused by a deviation in the test results as the test was ended when the punch was in contact with the sides of the bending sample. The test is then no longer frictionless and the results aren't accurate.

The fracture mechanism is crucial to explain the measured bending angles. Sarkar et al. showed in their study that certain factors aid the initiation of shear bands. These factors are small microcracks, initial surface roughness and hard. Microcracks are known to be introduced at large particles. These then further lead to the initiation of fracture. [21] The primary particles studied in section 4.4 are assumed affect the materials bendability.

The C24-X1 alloy systematically displays the best bendability as seen in Figure 5-9. The C20-Y1 alloy is seen to perform slightly better than C28-C2. The reason for this trend is hard to pinpoint. The primary particles in C28-C2 were seen to be larger than in the other alloys. This certainty has a negative effect on the bendability. The primary particles are also seen to be elongated in ED direction for all alloys. Why C24-X1 performs better than C20-Y1 is probably not linked to the size of the primary particles. Since the particles were seen to be larger in the former alloy. The high bendability is therefor likely due to the fibrous microstructure seen in the C24-X1 alloy.

5.3.2 Anisotropy in bendability

With the exception of C24-X1 T4, the highest bending angle reached in 90-orientation. The systematic trend is that the specimens oriented perpendicular to the extrusion direction (90) has the largest bending angle at fracture initiation stage. As the elongated primary particles follow the extrusion direction, they affect the anisotropy of the material. For the specimens orientated 90 degrees to the extrusion direction, a smaller surface area exists for the microcracks to initiate. This is believed to be the leading cause of this anisotropy.

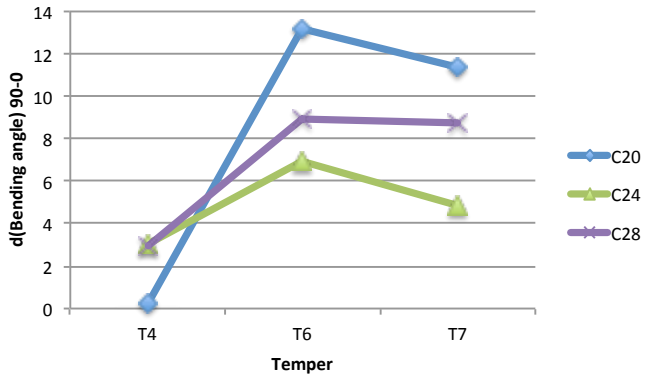

Figure 5-10: The difference in angle between the 90- and 0-orientations.

The anisotropy is lowest for the T4-temper state, the T6 state displays slightly more anisotropy than T7. In Figure 5-10 the difference in bending angle is calculated to illustrate

the anisotropy. The calculated difference is an absolute value. The C20-Y1 alloy shows highest difference in T6 and T7. The lowest difference in bending angle is seen for the C24-X1 alloy in these tempers.

5.3.3 Comparison of the different profiles

As the bendability of the box profiles and flat profiles are compared for the C20-Y1 and C24-X1 similarities are noticed. The highest bending angles α are reached by the C24-X1 alloy, for both the flat profile C24 T6 and the box profile V13-S0.

The difference in angle α between the 90- and 0-orientation is the highest for the C20 profiles. Both the box profile V7-S0 and the flat profile C20-Y1 display highest anisotropy.

Unlike the tensile properties discussed in section 5.2.4, the bendability of the flat profiles and box profiles seem to correspond for the respective alloys. Only the bendability of C24-X1 and C20-Y1 at T6 is considered and might not give a complete representation of the similarities and difference between the flat and box profile.

5.4 Correlation of bending and tensile tests.

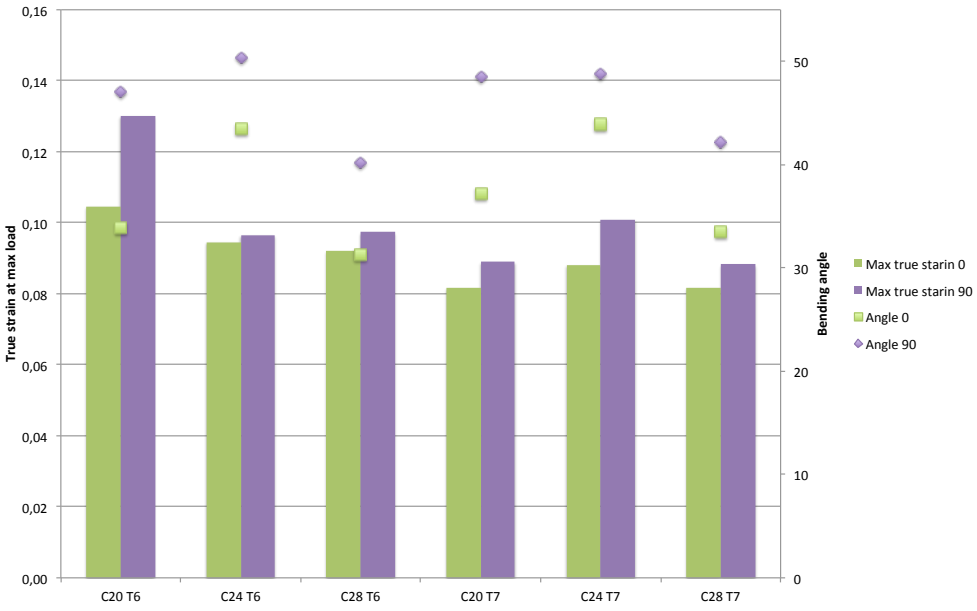

Figure 5-11: Bending angles and true strain at max load for T6 and T7.

In Figure 5-11 the results of the bending test are compared with the true strain at maximum load (Eu) of the T6- and T7-tempered materials. The T4-tempered materials are excluded as they are viewed to be inaccurate.

The first observation is the highest true strain and bending angle is reached in 90-orientation. There seems to be a clear correlation between the two mechanical tests. As mentioned before the high angles in the 90-orientation, is related to the elongated primary particles. The effect of the elongated particles on the tensile test is difficult to quantify, as the microstructure and the texture are likely to affect the mechanical properties as well.

5.5 Further Work

As many variables are present when studying the role of the alloying elements and the heat treatment on the extruded profiles, less time is left to go in detail on each specific subject area.

The precipitation sequence is presumed to play a vital role on the mechanical properties of the different profiles. A deeper investigation of precipitation sequence would give better understanding of the systematic difference for each alloy. Heat-treatment at different temperatures and time durations combined with hardness measurements would give clearer view of when the peak- and over-aged strength is reached. In addition study of the precipitates in a Transition Electron Microscope (TEM) would give additional information.

As good combination of ductility and strength is desired, fracture mechanism in the different alloys and directions is interesting study in detail. The study of the fracture surface in SEM is presumed to give more information about profiles. More parameters of ductility like elongation at fracture and reduction of area would aid in the research.

Also the role of the texture is interesting factor to further research. As the crystallographic texture is intricate subject matter, it is difficult to exactly connect the different texture components and strength to the mechanical properties. A comparison of texture-less profiles to the profiles chosen in this thesis would lead to further understanding the role of the texture.

6 Conclusions

Based on work completed in this thesis, several conclusion are made

- The C20-Y1 alloy is fully recrystallized, C24-X1 and C28-C2 have a fibrous microstructure.
- The recrystallized C20-Y1 showed a strong cube texture, and the fibrous displayed a deformation texture
- Large primary particles are seen in the C28-C2 alloy, which is connected with high amount alloying elements. The lowest average particle size is seen for the low alloyed C20-Y1 material. Generally the particles are seen to be elongated in the extrusion direction.
- The general trend shows the high-alloyed C28-C2 to be the strongest, followed by C24-Y1 and the weakest is seen to be low-alloyed C20-Y1.
- C28-C2 experiences a loss of in strength in the T7 state. The transition from peak-aged to over-aged occurs rapidly, presumably due to the fact C28-C2 has the highest amount of alloying elements.
- The true strain at max load (Eu) is seen to be similar for the two fibrous alloys C28-C2 and C24-X1, as the subgrain structure gives lower ductility. The recrystallized C20-Y1 systematically shows highest Eu.
- True strain at max load (Eu) of the recrystallized C20-Y1 is highly dependent on the temper state more so than the fibrous alloys, as a notable difference in Eu is seen for C20-Y1 T6 and C20-Y1 T7.
- For the tensile properties in the different orientation (0°, 45° and 90° to the extrusion direction) the strongest to weakest is shown: 45, 0 and 90 for the artificially aged materials. For the naturally aged T4 materials the order was seen to be: 0, 90 and 45. The Eu achieved in order form highest to lowest is seen as: 45, 90 and 0.
- The tensile test in different orientations (0°, 45° and 90° to the extrusion direction) shows highest anisotropy for the C20-Y1 alloy. A plausible reason is the combination of large grains and strong cube texture.
- The highest bending angles are reached by the C24-X1 alloy, followed by C20-Y1 and finally C28-C2. Good bendability is presumed to be due to a combination of microstructure and primary particles.
- The anisotropy in terms of difference between bending angles in the 0- and 90-orientions were seen to be largest for C20-Y1. The C24-X1 showed lowest anisotropy.

- The flat profiles reached the highest bending angles for both C20-Y1 and C24-X1. It is also noticed the flat profiles consistently achieved higher Eu.
- When correlating the bending and tensile properties, a similarity is seen as both highest bending angles and highest Eu was reached for the 90-oriented specimens. The primary particles elongated in the extrusion direction are expected to be the reason for these results.

7 References

1. Miller, W.S., et al., *Recent development in aluminium alloys for the automotive industry.* Materials Science and Engineering: A, 2000. **280**(1): p. 37-49.
2. S.Dumoulin, *Dynamic and quasi-static crash preformance of aluminium extrusions: summary of students screening tests*. 2013.
3. Sheppard, T., *Extrusion of aluminium alloys*. 1999, Dordrecht: Kluwer Academic. XII, 420 s. : ill.
4. Reiso, O. *Extrusion of AlMgSi alloys*. 2004. MATERIALS FORUM.
5. Dieter, G.E., *Mechanical metallurgy*. 1986, New York: McGraw-Hill. XXIII, 751 s. : ill.
6. Polmear, I.J., *Light alloys: from traditional alloys to nanocrystals*. 2006, Amsterdam: Elsevier. XIV, 421 s. : ill.
7. Verlinden, B. and R.W. Cahn, *Thermo-mechanical processing of metallic materials*. 2007, Amsterdam: Pergamon. 1 online resource (xxi, 528 s.) : ill.
8. Humphreys, F.J. and M. Hatherly, *Recrystallization and related annealing phenomena*. 2004, Amsterdam: Elsevier. xxx, 628 s. : ill. (some col.).
9. Solberg, J.K., *Lysmikroskopi*. 1998, [Trondheim]: Metallurgisk institutt. III, 97 s. : ill.
10. Pedersen, K.O., et al., *Strength and ductility of aluminium alloy AA7030.* Materials Science and Engineering: A, 2008. **473**(1–2): p. 81-89.
11. Yoshida, K., et al., *The effects of texture on formability of aluminum alloy sheets.* Acta Materialia, 2007. **55**(13): p. 4499-4506.
12. Holmedal, B., *Lecture notes in TMT 4266 "Metallforming - mikrostruktur og krystallplastisitet"* 2013.
13. Choi, C.-H. and D. Lee, *Evolution of recrystallization texture from aluminum sheet cold rolled under unlubricated condition.* Metallurgical and Materials Transactions A, 1997. **28**(11): p. 2217-2222.
14. Schwartz, A.J., *Electron backscatter diffraction in materials science*. 2009: Springer.
15. Hjelen, J., *Scanning elektron-mikroskopi*. 1989, Trondheim: SINTEF. 106 s. : ill.
16. ; Available from: http://ocw.mit.edu/courses/materials-science-and-engineering/3-11-mechanics-of-materials-fall-1999/modules/ss.pdf.
17. Dorward, R.C. and C. Bouvier, *A rationalization of factors affecting strength, ductility and toughness of AA6061-type Al–Mg–Si–(Cu) alloys.* Materials Science and Engineering: A, 1998. **254**(1): p. 33-44.
18. Vasudevan, A.K. and R.D. Doherty, *Grain boundary ductile fracture in precipitation hardened aluminum alloys.* Acta metallurgica, 1987. **35**(6): p. 1193-1219.
19. Neuhaus, R. and M. Borsutzki, *Plättchen-Biegeversuch nach VDA 238-100.* Materials Testing, 2013. **55**(9): p. 654-659.
20. Hu, J., Z. Marciniak, and J. Duncan, *Mechanics of Sheet Metal Forming*. 2002: Elsevier Science.
21. Sarkar, J., et al., *Tensile properties and bendability of T4 treated AA6111 aluminum alloys.* Materials Science and Engineering: A, 2004. **369**(1–2): p. 258-266.

Appendices

Appendix A – Surface layer microstructure by EBSD.

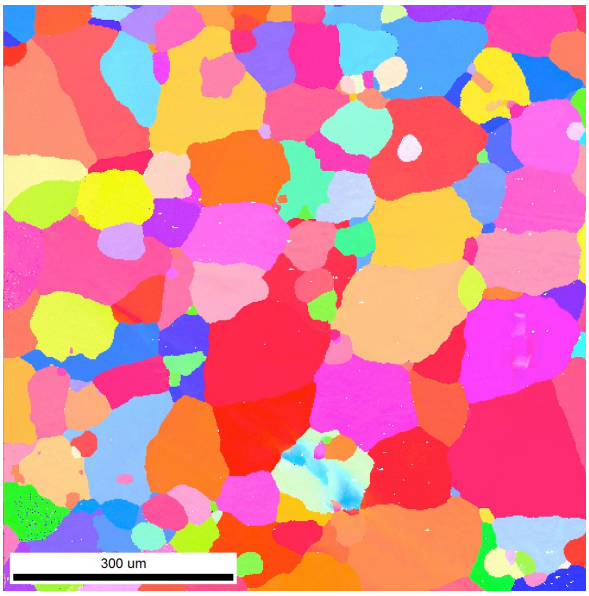

Figure A-1: The ED-TD cross-section of C20-Y1.

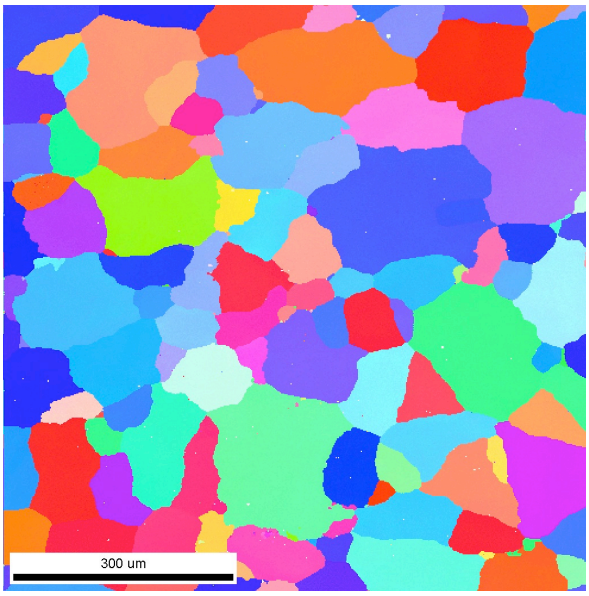

Figure A-2: The ED-TD cross-section of C24-X1.

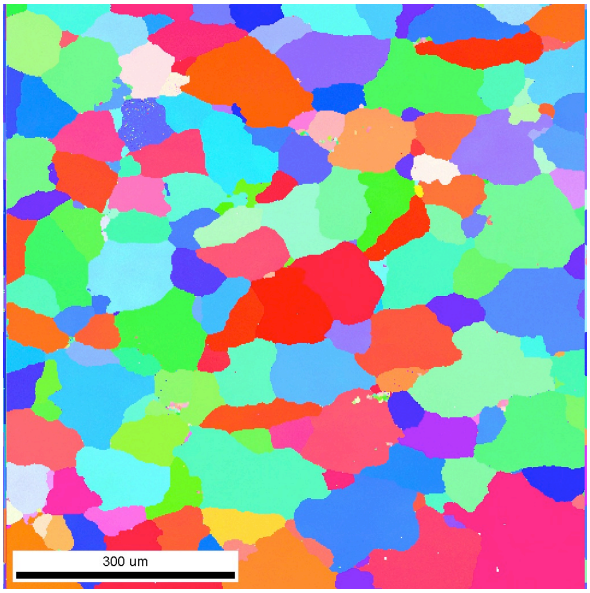

Figure A-3: The ED-TD cross-section of C28-C2.

Appendix B – Stress-strain curves W/T4 tempered materials.

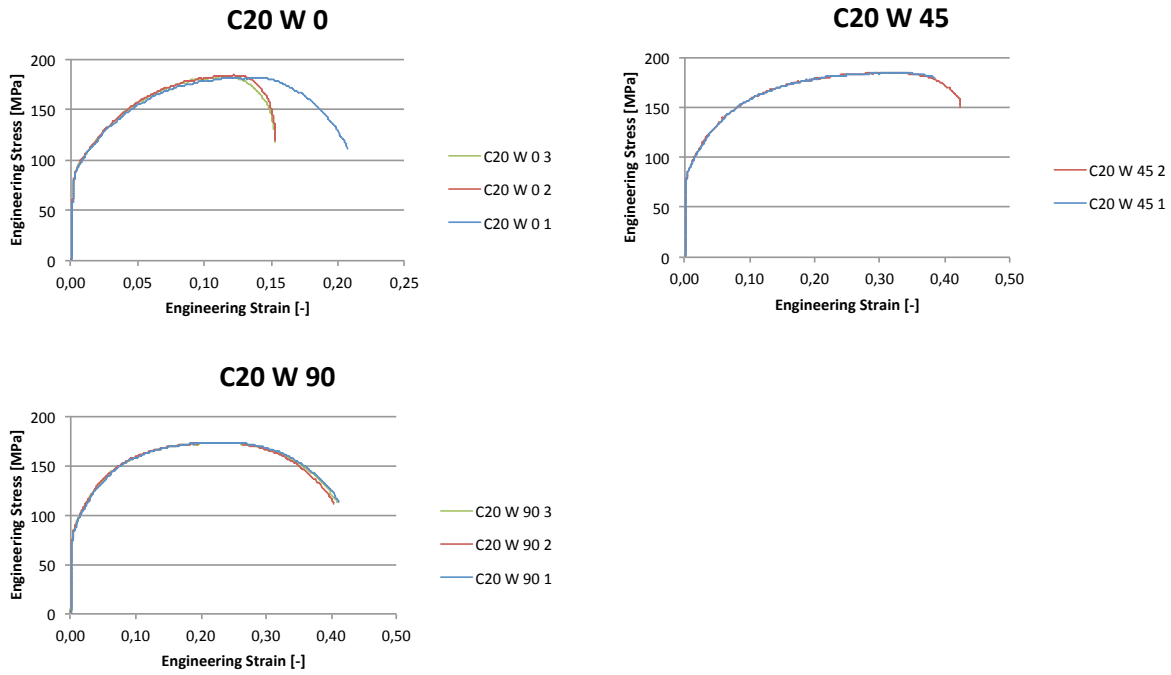

Figure B-1: Stress-strain curves of C20-Y1.

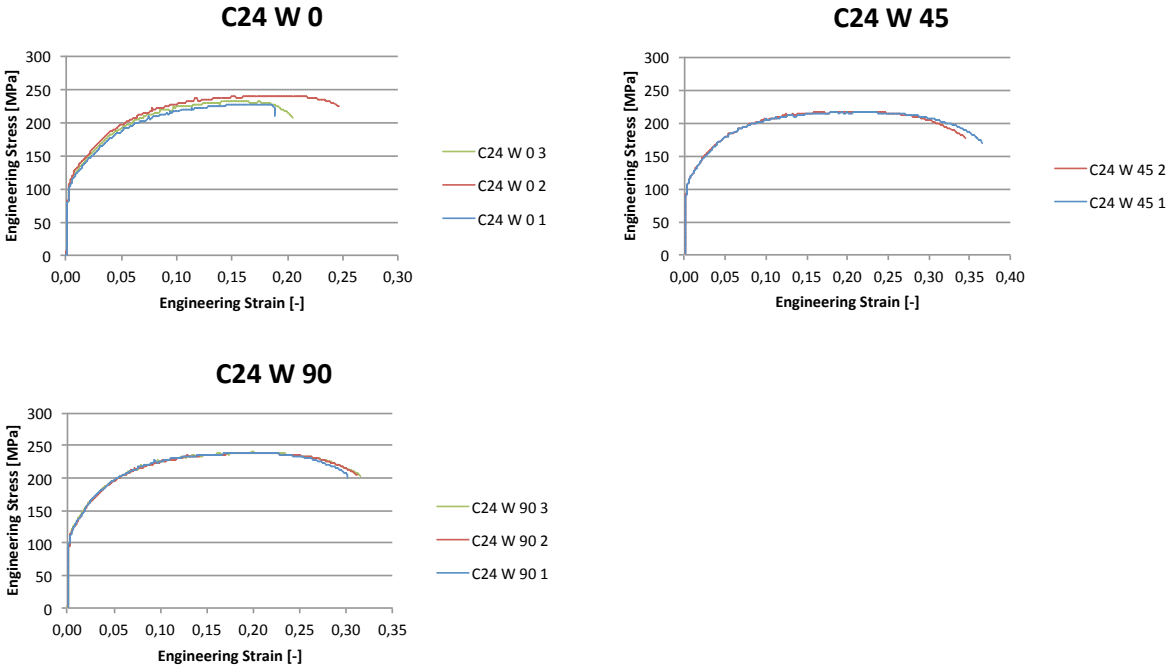

Figure B-2: Stress-strain curves of C24-X1.

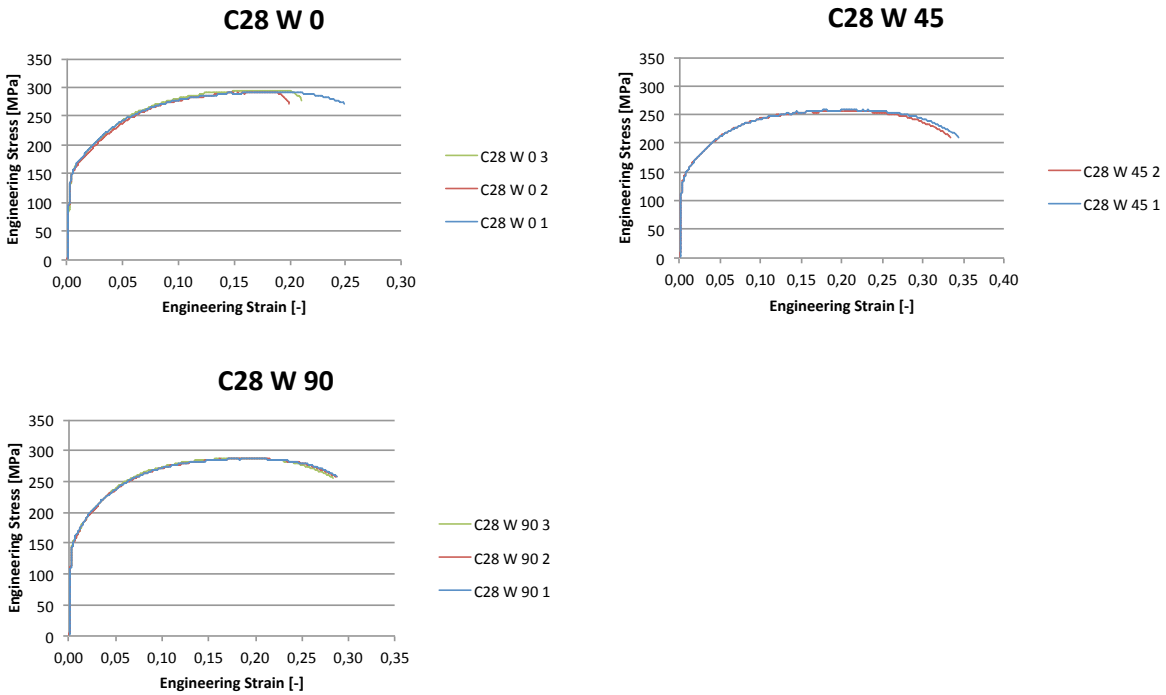

Figure B-3: Stress-strain curves of C28-C2.

Appendix C – Force-extension curves

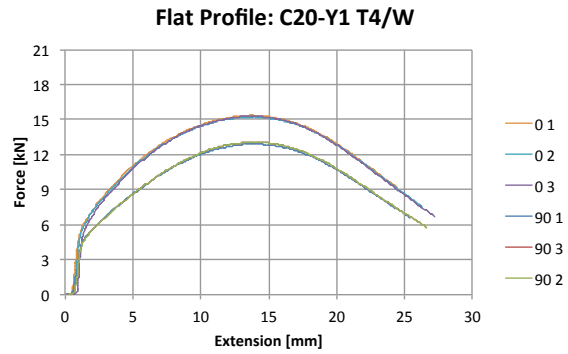

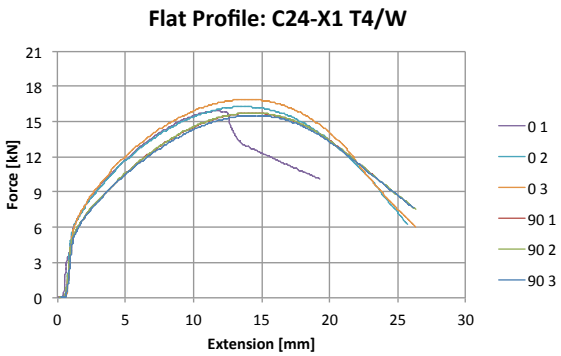

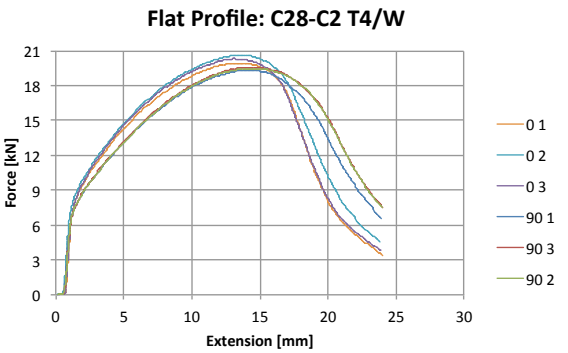

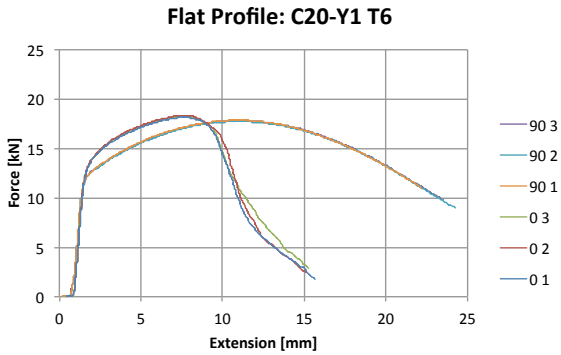

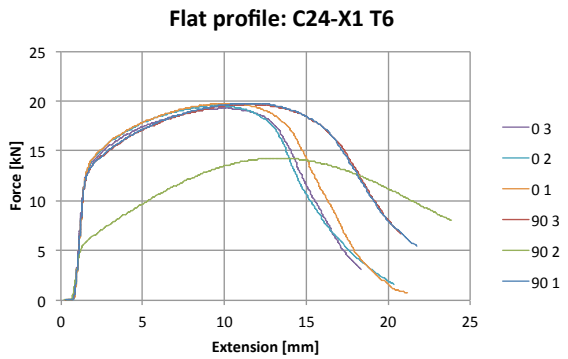

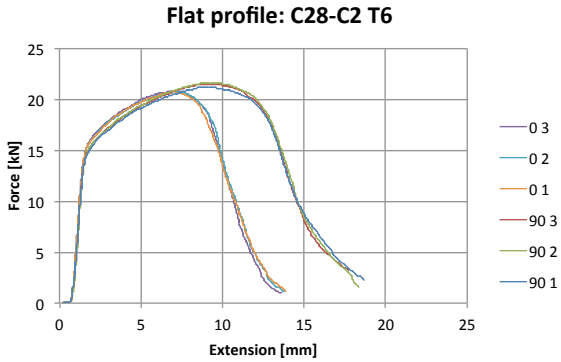

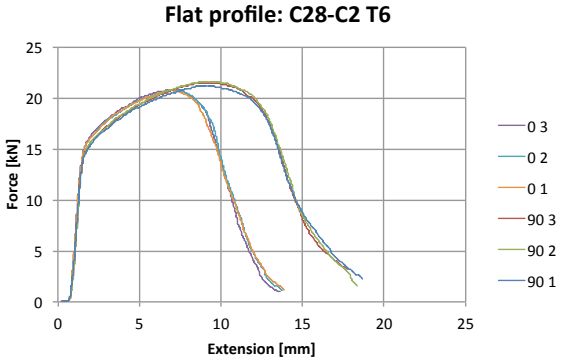

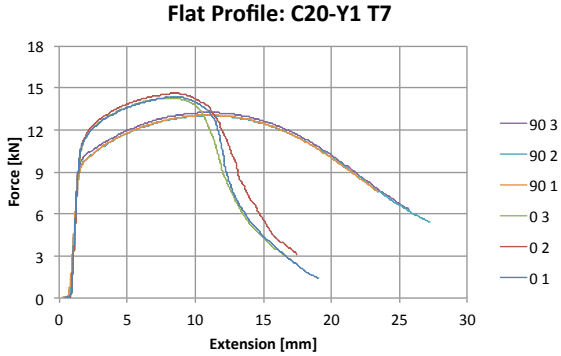

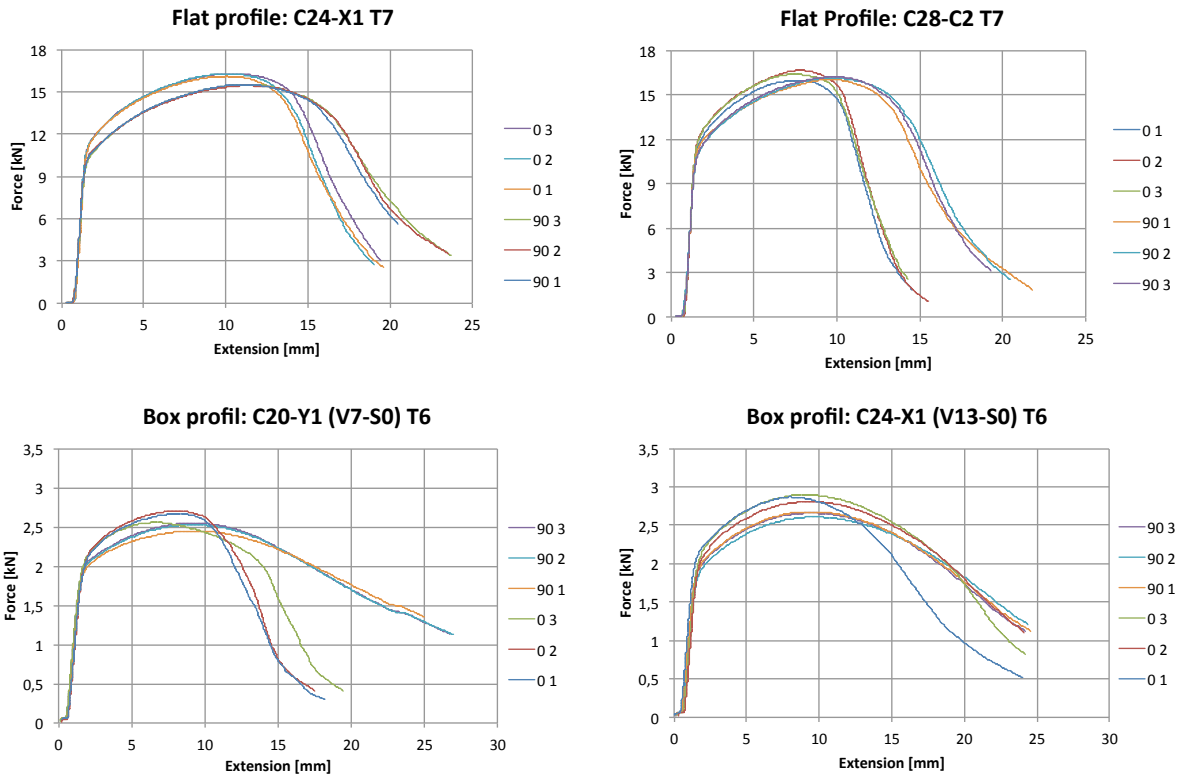

Figure C-1: Bending test- Force-Extension curves.